

Ab Initio Surface Chemistry with Chemical Accuracy: Application to Water on Metal Oxides

Hong-Zhou Ye^{1, a)} and Timothy C. Berkelbach^{1, b)}

Department of Chemistry, Columbia University, New York, NY 10027 USA

First-principles calculations are a cornerstone of modern surface science and heterogeneous catalysis. However, accurate reaction energies and barrier heights are frequently inaccessible due to the approximations demanded by the large number of atoms. Here we combine developments in local correlation and periodic correlated wavefunction theory to solve the many-electron Schrödinger equation for molecules on surfaces with chemical accuracy, commonly defined as 1 kcal/mol. As a demonstration, we study water on the surface of Al_2O_3 and TiO_2 , two prototypical and industrially important metal oxides for which we obtain converged energies at the level of coupled-cluster theory with single, double, and perturbative triple excitations [CCSD(T)], commonly known as the “gold-standard” in molecular quantum chemistry. We definitively resolve the energetics associated with water adsorption and dissociation, enabling us to address recent experiments and to analyze the errors of more commonly used approximate theories.

I. INTRODUCTION

The structure, bonding, and chemistry of molecules and materials is governed by the many-electron Schrödinger equation, which, for all but the simplest systems, must be solved approximately using numerical techniques. Especially for solids and surfaces, containing a semi-infinite number of atoms, severe approximations have historically been necessary, and a primary effort of computational materials science has been the gradual elimination of these approximations. Early work used noninteracting and mean-field theories of band structure, evolving into the popular density functional theory (DFT), all of which reduce the many-electron Schrödinger equation to a set of self-consistent one-electron Schrödinger equations. However, the limitations of DFT have been noted in the context of chemical reactions,^{1,2} surface adsorption,^{3,4} and heterogeneous catalysis,^{5–7} encouraging the development of more accurate methods applicable to complex systems epitomized by molecules on periodic solid surfaces.

To go beyond one-electron theories, explicit electron correlations can be reintroduced with finite- or infinite-order perturbation theories that can, in principle, be systematically converged to a numerically exact solution. Here, we show that, with new methodological developments, this convergence can be achieved along all necessary axes—including the description of electron correlation, the one-electron basis set, and the size of the model surface—to provide surface chemistry energetics with chemical accuracy, comparable to that which is achievable for small-molecule main-group chemistry.^{8,9} Specifically, as our highest level of theory, we apply coupled-cluster theory with single, double, and perturbative triple excitations [CCSD(T)],¹⁰ commonly known as the “gold standard” in molecular quantum chemistry. The application of such methods to solids can be traced back to 1990s^{11,12} and has been increasingly pursued over the last few years.^{13–24} We leverage several recent developments in periodic integral evaluation^{25–27} and Gaussian basis sets²⁸ along with a new implementation of periodic CCSD(T) with local

correlation to enable a quantitative study of single molecule adsorption and reaction chemistry on solid surfaces at this high level of theory.

II. COMPUTATIONAL METHODS

Within the Born-Oppenheimer approximation, the total electronic energy is expressed as a sum of the Hartree-Fock energy and the correlation energy, $E = E_0 + E_c$. We first calculate the Hartree-Fock energy using large supercells with periodic boundary conditions. We then use a local, fragment-based approach wherein the correlation energy of a supercell containing N electrons is expressed as a sum of contributions from all N localized occupied orbitals i , $E_c = \sum_{i=1}^N E_c^{(i)}$. Importantly, each contribution $E_c^{(i)}$ is evaluated independently in a truncated set of occupied and unoccupied orbitals that are optimized for local orbital i ; specifically, we use local natural orbitals (LNOs) from second-order perturbation theory^{29,30} with periodic boundary conditions. For the insulating materials studied here, the number of LNOs needed for a target accuracy is independent of the total system size. Thus, the cost of calculating the total correlation energy grows only linearly with N and each calculation of $E_c^{(i)}$ is independent of all others, which enables highly efficient simulation of large systems through parallel computing. By increasing the number of LNOs, we converge to the exact periodic CCSD(T) energy at a fraction of the cost. This low cost allows us to simulate periodic solids with supercells containing over 100 atoms and almost 1000 electrons using high-quality correlation-consistent one-electron basis sets²⁸ and thus to reliably eliminate errors stemming from incomplete basis sets, cluster models, or small simulation cells. Details of our computational methods are provided in the Supplementary Material.

III. WATER ON METAL OXIDES

As a demonstrative application of these developments, we study the interaction between water and solid metal oxides, which are two of the most abundant substances on Earth.

^{a)}Electronic mail: hzyechem@gmail.com

^{b)}Electronic mail: t.berkelbach@columbia.edu

Understanding the chemistry of their interaction is important for myriad technological applications, including electronics, catalysis, and corrosion.^{31–33} For example, semiconducting metal oxides such as TiO_2 are popular photocatalysts for solar water splitting.^{34,35} The chemistry of water on metal oxide surfaces also serves as an important model for general surface chemistry and heterogeneous catalysis, motivating extensive experimental and theoretical research efforts,^{32,36–38} with experiments primarily performed using temperature-programmed desorption,^{39,40} vibrational sum frequency generation,⁴¹ and scanning probe microscopies.^{42,43} Specifically, we study Al_2O_3 and TiO_2 , two prototypical metal oxides and subjects of ongoing debates about the fate of a molecularly adsorbed water molecule,^{38,40,43} which we aim to resolve in the present work.

We first consider Al_2O_3 , which is a common support in heterogeneous catalysis and has been intensively studied as a model metal-oxide surface for water reactivity.^{23,36,37,40,44} In particular, the most stable α - Al_2O_3 (0001) surface has been characterized, computationally by DFT and experimentally under ultrahigh vacuum, to be aluminum-terminated with significant structural distortions.

Water undergoes molecular adsorption through an interaction between the water molecule’s oxygen lone pair and a three-fold coordinated surface aluminum, after which it can potentially dissociate, transferring a hydrogen atom to a neighboring surface oxygen atom, yielding OH_{ads} and OH_{surf} fragments (Fig. 1A). DFT calculations spanning 25 years^{36,44–46} all predict that dissociation is favorable by about 10 kcal/mol, with a small barrier of about 4 kcal/mol, suggesting fast and complete dissociation within a few nanoseconds at room temperature (Fig. 1B). The first experimental support for this process came in 2014 by observing signatures of surface hydroxyls in vibrational spectroscopy.³⁷ However, later experiments using vibrational spectroscopy and temperature-programmed desorption found that the dissociated products can take days to form even in ambient conditions.^{40,41} This timescale is in stark contrast to the small reaction barrier predicted by DFT, highlighting the challenge of studying elementary chemical reactions on well-defined surfaces and raising questions about the origin of this discrepancy.

With high-level periodic quantum chemistry methods in hand, we can accurately quantify the surface reaction energetics, which must be carefully converged with respect to the number of correlated orbitals, the basis set size, the surface size, and the slab thickness (Fig. 1C–H). All geometries were optimized using DFT with the popular Perdew-Burke-Ernzerhof (PBE) functional⁴⁷ and the D3 dispersion correction⁴⁸ (PBE+D3), which was used by previous theoretical studies of the same system,⁴⁴ and further details are provided in the Supplementary Material. Figure 1C visualizes the unoccupied LNO subspace for a representative localized occupied orbital, where the number of LNOs can be increased systematically by tightening the truncation threshold. Figure 1D shows the convergence of the LNO-CCSD(T) reaction energy and barrier height for a small 1×1 surface model containing six atomic layers ($6\text{L}/1 \times 1$) with a triple-zeta (TZ) basis set, which is the largest system where canonical CCSD(T) re-

sults can be generated for comparison. Both energies are seen to converge quickly to the canonical results within chemical accuracy by using less than 100 LNOs per occupied orbital, which is a small fraction of the total number of orbitals (about 630). This fast convergence is consistent with the large gap of Al_2O_3 and its weakly correlated, main-group electronic structure. As shown in Fig. 1F, the smaller number of LNOs results in significant speedups of CCSD(T); for the large basis sets necessary to eliminate basis set incompleteness errors, the speedup is more than a factor of 100. This high computational efficiency allows us to apply LNO-CCSD(T) to much larger surface models beyond the reach of canonical CCSD(T), as exemplified in Fig. 1E for a $12\text{L}/2 \times 2$ surface model that contains over 80 atoms and 2000 orbitals in the TZ basis. The LNO-CCSD(T) energies again show quick convergence, requiring a number of LNOs comparable to that of the smaller system, demonstrating the ability to scale to large systems without the significant increase in cost that accompanies canonical CCSD(T). We are thus able to fully converge the reaction energy and barrier height with respect to the surface size, basis set size (Fig. 1G), and slab thickness (Fig. 1H). We have used the same method to calculate the adsorption energy, using a counterpoise correction for basis set superposition error.

Our final results obtained using periodic LNO-CCSD(T) are presented in Fig. 2A, where they are compared to those obtained using several other levels of theory. All energies have been corrected by the vibrational zero-point energy (ZPE) evaluated using PBE, which yields non-negligible corrections of -0.4 kcal/mol for the magnitude of the adsorption energy, -0.6 kcal/mol for the dissociation reaction energy, and -2.2 kcal/mol for the barrier height. CCSD(T) predicts a sizable adsorption energy of 26.5 kcal/mol, while PBE+D3 overestimates this number by about 3 kcal/mol. This trend is consistent with that observed previously for water adsorption on the MgO (001) surface.²¹ CCSD(T) also confirms that the dissociative adsorption product predicted by PBE+D3 is thermodynamically more stable than the molecularly adsorbed water by about 8 kcal/mol. The dissociation energy of molecularly adsorbed water is -7.5 kcal/mol from CCSD(T), which is in good agreement with the value of -8.6 kcal/mol from PBE+D3. However, the reaction barrier height from CCSD(T) is 6.6 kcal/mol, which is more than twice that predicted by PBE+D3 (2.8 kcal/mol, i.e., an underestimation by almost 4 kcal/mol).

The underestimation of reaction barriers by DFT with a generalized gradient approximation (GGA) functional like PBE is well-known and can be traced back to the systematic self-interaction error (SIE) of semilocal functionals.¹ In Fig. 2A, we also show the reaction energetics obtained using DFT with a meta-GGA functional, SCAN⁴⁹+D3, a hybrid functional, PBE0⁵⁰+D3, and the second-order Møller-Plesset perturbation theory, MP2. The two functionals mitigate the SIE by satisfying more exact constraints on the exchange-correlation functional⁴⁹ (SCAN) or through partial inclusion of the exact exchange energy² (PBE0), while MP2 completely removes the SIE and includes approximate many-body electron correlation to second order. All three methods are seen

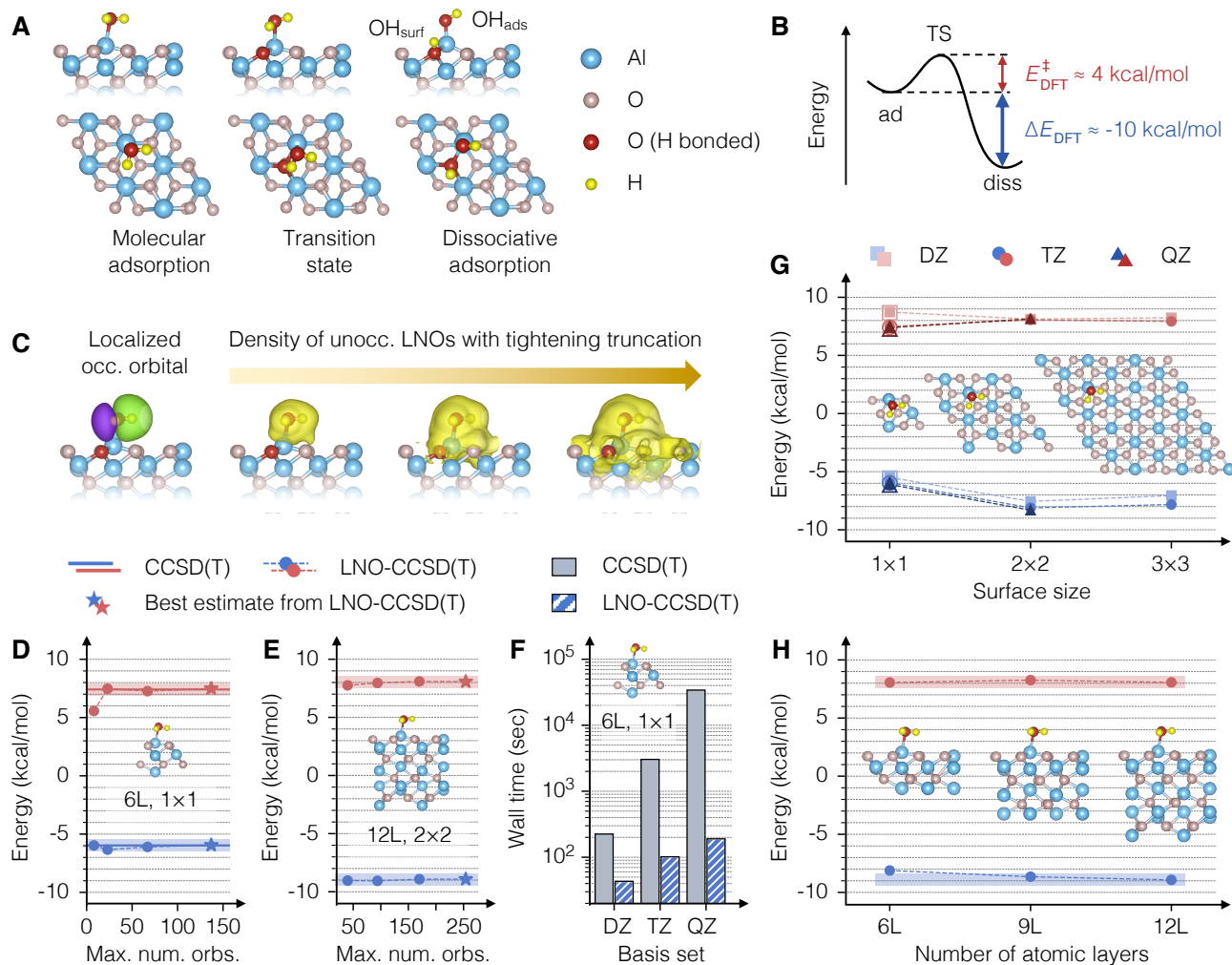


FIG. 1. (A) Atomic structure of a single water molecule adsorbed on the α - $\text{Al}_2\text{O}_3(0001)$ surface. The molecularly adsorbed water molecule (left) may transfer a hydrogen to a neighboring surface oxygen via the transition state (middle), resulting in OH_{ads} and OH_{surf} fragments (right). (B) Schematic illustration of the potential energy surface associated with the water dissociation reaction predicted by DFT. (C) Isosurface visualization of a representative localized occupied orbital and the density of the corresponding unoccupied LNOs, the number of which increases with tightening truncation threshold (left to right). (D) The convergence of the reaction energy (blue) and barrier (red) calculated by LNO-CCSD(T) with the LNO subspace size for a small surface model of 6 atomic layers and 1×1 surface using a TZ basis set. With about 100 LNOs per occupied orbital, the LNO-CCSD(T) energies converge to the canonical CCSD(T) results (solid horizontal line) to an accuracy better than 1 kcal/mol (shaded area). (E) The same as in (D), but for a larger surface model with 12 atomic layers and 2×2 surface size, where canonical CCSD(T) is unavailable. (F) Wall time of LNO-CCSD(T) calculations for the 6L/ 1×1 surface model using basis sets of increasing size compared to canonical CCSD(T). (G) Reaction energy (blue) and barrier (red) calculated by LNO-CCSD(T) for a 6L slab with increasing surface size and basis set size. The canonical CCSD(T) results are also shown in hollow markers for the 1×1 surface. Both energies are converged to better than 1 kcal/mol of accuracy using a 2×2 surface and a TZ basis set. (H) Reaction energy (blue) and barrier (red) calculated by LNO-CCSD(T) in a TZ basis set for a 2×2 surface with increasing slab thickness. Both energies are converged to better than 1 kcal/mol of accuracy using a 12L model.

to improve upon PBE+D3 in the calculated reaction barrier, predicting barriers of 4.0 kcal/mol (SCAN+D3), 4.5 kcal/mol (PBE0+D3), and 5.6 kcal/mol (MP2). However, SCAN+D3 and PBE0+D3 show even stronger overestimation of the adsorption energy compared to PBE+D3, highlighting the challenge of designing a universal functional for surface chemistry, while the wavefunction-based MP2 theory agrees quantitatively with CCSD(T).

The higher barrier predicted by CCSD(T) has a signif-

icant impact on the kinetics of the surface reaction over a wide range of temperature. We approximate the reaction rate using harmonic transition state theory,⁵¹ $k(T) = (k_{\text{B}}T/h) \exp\{-[\Delta E^{\ddagger} + \Delta F_{\text{vib}}^{\ddagger}(T)]/k_{\text{B}}T\}$, where h is Planck's constant, k_{B} is Boltzmann's constant, T is temperature, ΔE^{\ddagger} is the reaction barrier without ZPE correction, and $\Delta F_{\text{vib}}^{\ddagger}(T)$ is the temperature-dependent vibrational activation free energy, which we calculated using harmonic frequencies from PBE (the vibrational correction to the barrier height is reduced

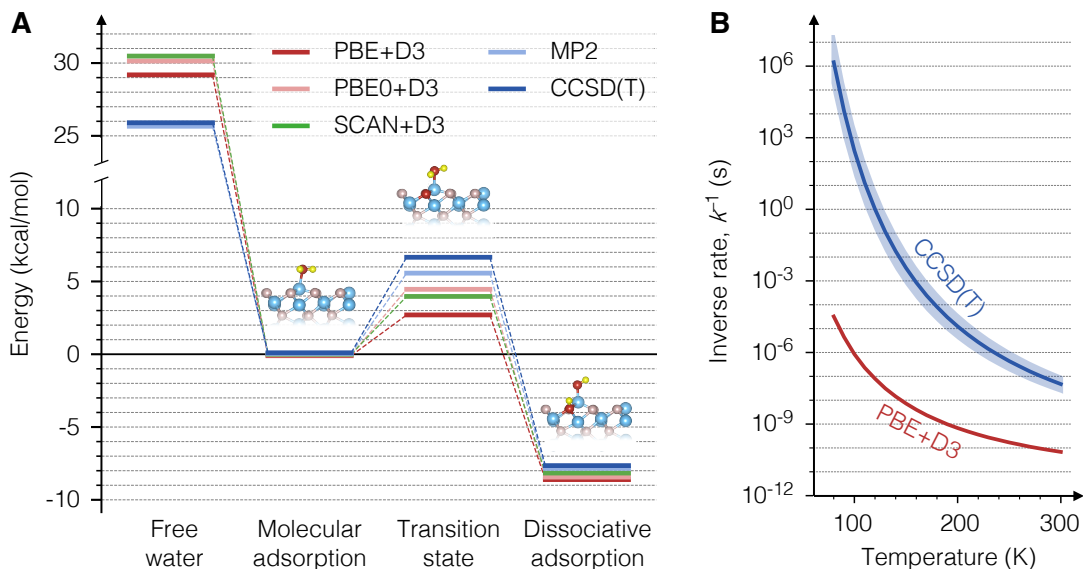


FIG. 2. (A) Zero-point energy corrected reaction energetics associated with the water adsorption and dissociation reaction calculated using different electronic structure methods. (B) Inverse rate for the water dissociation reaction in the temperature range of 80 K to 300 K evaluated using harmonic transition state theory. For CCSD(T), the shaded area indicates an energy uncertainty of ± 0.5 kcal/mol.

in magnitude from -2.2 kcal/mol at 0 K to -1.4 kcal/mol at 300 K; see Fig. S4 in the Supplementary Material). The reaction timescales using CCSD(T) and PBE+D3 barrier heights are shown in Fig. 2B for the temperature range of 80–300 K.

At 300 K, all levels of theory predict the dissociation of the water O-H bond to be fast on the surface, with CCSD(T) predicting $k^{-1} \approx 0.1 \mu\text{s}$, which is three orders of magnitude slower than $k^{-1} \approx 0.1$ ns from PBE+D3. The difference between CCSD(T) and PBE+D3 becomes even more prominent at lower temperature. At 80–100 K, PBE+D3 still predicts fast dissociation with $k^{-1} \approx 1 \mu\text{s}$. By contrast, CCSD(T) predicts slow kinetics with a time scale of about a day, i.e., about nine orders of magnitude slower than that predicted by PBE+D3. While the slow kinetics at about 100 K predicted by the CCSD(T) barrier height are consistent with cryogenic data,⁴⁰ the prediction at 300 K does not agree with experiments performed at room temperature.⁴¹

Although classical transition state theory is approximate, due to its neglect of recrossing events and quantum tunnelling,⁵¹ it is highly unlikely that these corrections would be large enough⁴⁶ to predict a lifetime consistent with room-temperature experiments,⁴¹ especially in ultrahigh vacuum. Therefore, we conclude that unimolecular adsorption and dissociation of water on a pristine $\alpha\text{-Al}_2\text{O}_3(0001)$ surface requires about a day at 100 K, but should occur by this mechanism on the sub-microsecond time scale at 300 K. We also predict the dissociation to be essentially irreversible: at 300 K, we predict $k^{-1} \approx 10$ s for the recombination of the two surface hydroxyl groups, which is 10^8 times slower than the dissociation reaction. Deviations seen in experiment must be associated with mechanisms not considered here, such as alternative surface motifs, competing reaction pathways, or cooperative effects.⁴⁰ However, even in the presence of alternative pathways, our predicted reaction timescale should be an up-

per bound to the one observed, and so understanding why our studied reaction path is not the one realized in experiments is unclear. For our studied reaction path, inaccuracies of the electronic structure theory, which we have shown to be large with common density functional approximations, have been eliminated by our work. Within the approximations of transition state theory, the reaction barrier needed to explain a reaction timescale on the order of days at room temperature is more than 25 kcal/mol; for CCSD(T) to be so wrong would be unprecedented.

To further explore the performance of CCSD(T) for surface reactions, we study TiO_2 , which has a more complicated electronic structure due to the 3d electrons of the transition metal Ti. The water- TiO_2 interface has been a focus of intensive research activities since the 1970s for its importance in photocatalytic water splitting for hydrogen generation.^{34,35} Particularly, the most stable rutile $\text{TiO}_2(110)$ surface has been characterized, computationally by DFT and experimentally under ultrahigh vacuum, to be terminated by alternating rows of five-fold coordinated titaniums (Ti_{5c}) and bridging oxygens (O_b). Water undergoes molecular adsorption via interaction of its lone pair with Ti_{5c} and a weak hydrogen bond with a neighboring O_b .

Like for Al_2O_3 , the possibility of subsequent dissociative adsorption is debated—not only the kinetics but also the thermodynamics. The hypothesized dissociation occurs through water transferring a proton to its neighboring O_b , yielding OH_{ads} and OH_{surf} fragments (Fig. 3A). Controversial results were seen in early experimental studies, wherein temperature-programmed desorption⁵⁴ and scanning tunneling microscope^{42,55} experiments found signals of only molecularly adsorbed water in the absence of surface defects, while photoemission spectroscopy⁵⁶ observed signatures of OH_{surf} and supported mixed molecular and disso-

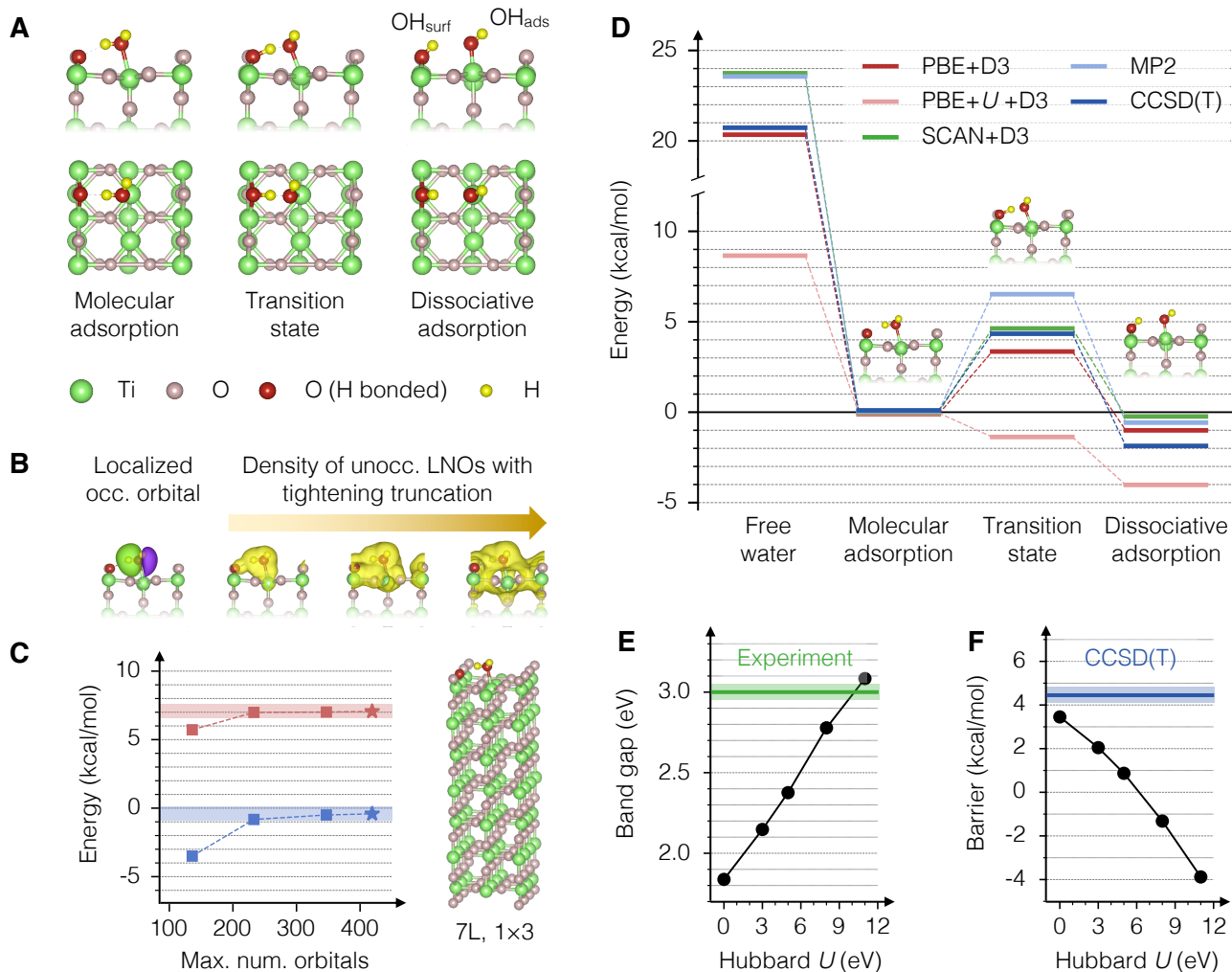


FIG. 3. (A) Atomic structure of a single water molecule adsorbed on the rutile $\text{TiO}_2(110)$ surface (left), which may transfer a hydrogen to a neighboring surface oxygen via the transition state (middle), leaving OH_{ads} and OH_{surf} fragments (right). (B) Isosurface visualization of a representative localized occupied orbital and the density of the corresponding unoccupied LNOs obtained with tightening truncation (left to right). (C) The convergence of the LNO-CCSD(T) reaction energy (blue) and barrier (red) with the LNO subspace size for a $7\text{L}/1 \times 3$ model using a TZ basis set. Both energies are converged to an accuracy better than 1 kcal/mol (shaded area) with about 300 LNOs per occupied orbital, which is a small fraction of the total orbital count (about 5000). (D) ZPE-corrected reaction energetics associated with the water adsorption and dissociation reaction calculated using different electronic structure methods. For PBE+ U , $U = 8$ eV is applied to the $3d$ band of Ti as suggested by previous work.⁵² (E) Band gap of bulk rutile TiO_2 predicted by PBE+ U with different values of U , compared with the experimental value.⁵³ (F) ZPE-corrected barrier height for the water dissociation predicted by PBE+ U +D3 with different values of U , compared with the CCSD(T) reference.

ciative adsorption. In a recent combined scanning tunneling microscope-molecular beam experiment, dissociative adsorption on the Ti_{5c} site was measured at very low water coverage to be slightly higher in energy than molecular adsorption by 0.8 kcal/mol, with a barrier height of 8.3 kcal/mol.⁴³ Early DFT calculations found conflicting predictions on the relative stability of the two adsorption states,^{55,57,58} where results depend sensitively on choices of approximate functionals,^{59,60} dispersion corrections,⁶¹ and treatments of strong electron correlation.^{52,61} More recent DFT-based studies employing the SCAN functional along with machine learning potentials to enable molecular dynamics simulation found that dissociative adsorption is higher in energy by 0.5–1 kcal/mol,^{62,63} in

agreement with the recent experiment.⁴³ However, the barrier height was predicted to be about 6 kcal/mol,⁶³ which is more than 2 kcal/mol lower than the experiment.

We revisit this problem with periodic LNO-CCSD(T) for an isolated water molecule on the rutile $\text{TiO}_2(110)$ surface. Despite the more strongly correlated electronic structure of a transition metal oxide, the LNOs are well-localized around their associated localized occupied orbital (Fig. 3B). We have performed a convergence study analogous to that for Al_2O_3 and determined that, based on PBE+D3 calculations (Fig. S6), the surface chemistry energetics can be converged using a $7\text{L}/1 \times 3$ surface model (Fig. 3C) that contains about 130 atoms and 5000 orbitals when using a TZ basis set and that

the CCSD(T) calculations require about 300 LNOs per occupied orbital. Our final ZPE-corrected adsorption and reaction energetics are presented in Fig. 3D, where they are compared to DFT using PBE+D3 and SCAN+D3.

Our CCSD(T) calculations predict a ZPE-corrected adsorption energy of 20.8 kcal/mol, which is in excellent agreement with the 20–22 kcal/mol heat of adsorption determined by temperature-programmed desorption experiments.^{54,64} Our adsorption energy is also in good agreement with a previous local CCSD(T) calculation that used an embedded cluster approach,¹⁸ but it is smaller in magnitude, by about 8 kcal/mol, than a more recent periodic CCSD(T) calculation that used a local embedding approach.⁶⁵ Both SCAN+D3 and MP2 overestimate our CCSD(T) energy by 3 kcal/mol, while PBE+D3 agrees with CCSD(T) within chemical accuracy.

For the surface water dissociation, CCSD(T) predicts dissociative adsorption to be slightly lower in energy than molecular adsorption by 1.9 kcal/mol, with a barrier height of 4.3 kcal/mol. Compared to the recent experimental estimation,⁴³ these numbers correspond to an overstabilization of the dissociation product by about 3 kcal/mol and an underestimation of the barrier height by about 4 kcal/mol. Like for the case of water on Al_2O_3 , the comparison between calculations and experiment is clearly a challenge, which we will discuss further in the Conclusions, but by taking the CCSD(T) results as a reference, we can evaluate the accuracy of lower levels of theory. Both PBE+D3 and SCAN+D3 yield a reaction profile similar to that of CCSD(T), predicting that dissociation is favorable by 1 kcal/mol from PBE+D3 and 0.2 kcal/mol from SCAN+D3, and a barrier height of 3.4 kcal/mol from PBE+D3 and 4.6 kcal/mol from SCAN+D3. By contrast, MP2 overestimates the barrier by about 2 kcal/mol and underestimates the dissociation energy by about 1.5 kcal/mol, suggesting that third- and higher-order electron correlation effects play an important role in the water-TiO₂ chemistry.

A common approach to improving the performance of semilocal functionals like PBE, especially in transition-metal containing materials, is the DFT+ U method.⁶⁶ For TiO₂, this method introduces a local Coulomb interaction to the Ti 3*d* atomic orbital, raising the energy of the Ti 3*d* band and yielding an increased band gap in better agreement with experiment. For bulk rutile TiO₂, the experimental band gap is about 3.0 eV and PBE predicts 1.8 eV; PBE+ U with the value $U = 8$ eV predicts 2.9 eV.⁵² Applying the same approach to the water dissociation reaction, we find that it worsens agreement with CCSD(T): it predicts an exoergic reaction by about 4.0 kcal/mol and a negative reaction barrier of -1.4 kcal/mol (Fig. 3D). This behavior can be understood by considering the bonding of the molecularly adsorbed water molecule. Raising the energy of the empty accepting Ti 3*d* orbital weakens the bond and destabilizes the molecularly adsorbed water, hence leading to a smaller barrier height and a more exoergic reaction. This also explains the significantly smaller adsorption energy predicted by PBE+ U +D3 (8.7 kcal/mol), also shown in Fig. 3D.

In Fig. 3E and F, we show the bulk band gap and the water dissociation barrier height as a function of the parameter U . Improving one worsens the other, and there is no single value

of U that accurately predicts both properties. This competing behavior is typical of DFT³ and highlights the challenge of using DFT for computational heterogeneous catalysis, where stretched bonds, dispersion, and strong correlation are all important. By contrast, high-level quantum chemical wavefunction approaches, such as CCSD(T), offer balanced and unbiased treatments of many-body electron correlation without empirical parameters.

IV. CONCLUSIONS

To summarize, we computationally investigated the chemistry of water on two prototypical metal-oxide surfaces, Al_2O_3 and TiO₂, using state-of-the-art periodic quantum chemistry at the CCSD(T) level of theory. The quantitative reaction energetics made possible by this work sheds new light on the long-standing puzzles between previous computational studies and experimental observations regarding the chemical equilibrium and kinetics of water molecules on these surfaces. Perhaps most significantly, we have shown that accurate barrier heights and reaction energies based on ZPE-corrected single-point energies do not provide quantitative agreement with those inferred from experiments. With CCSD(T), we believe that inaccuracies in the electronic structure are no longer responsible for the disagreement. Instead, we propose that reconciling calculations and experiments requires a consideration of more complex reaction networks, thermodynamic and dynamic effects not captured by the harmonic approximation and transition state theory, or a reevaluation of experiments. The results of our high-level quantum chemistry calculations also allowed an unbiased examination of the performance of DFT for elementary steps of reactions on real surfaces, for which comparisons to experiment are extremely challenging. Such accurate calculations can immediately be used for validation, selection, or design of more affordable density functional approximations or as training data for machine learning of force fields,^{67–69} which could be used in molecular dynamics simulations to explore thermodynamic effects not captured by single-point calculations.^{62,63} Although alternatives to CCSD(T) for multiconfigurational electronic structure of strongly correlated solids must be pursued,⁶ we anticipate that high-level periodic quantum chemistry approaches will play an increasingly important role in the toolbox of surface science. The large system sizes needed for convergence essentially demand the use of local correlation methods, such as the one used here.

ACKNOWLEDGEMENTS

We thank Garnet Chan, Sandeep Sharma, and Yifan Li for useful discussions. T.C.B. acknowledges the hospitality of the Center for Computational Quantum Physics, Flatiron Institute, where a portion of this work was completed. The Flatiron Institute is a division of the Simons Foundation. This work was supported by the National Science Foundation under Grant Nos. OAC-1931321 and CHE-1848369.

We acknowledge computing resources from Columbia University's Shared Research Computing Facility project, which is supported by NIH Research Facility Improvement Grant 1G20RR030893-01, and associated funds from the New York State Empire State Development, Division of Science Technology and Innovation (NYSTAR) Contract C090171, both awarded April 15, 2010. Crystal structures and electronic orbitals were visualized using VESTA.⁷⁰

- ¹A. J. Cohen, P. Mori-Sánchez, and W. Yang, *Chem. Rev.* **112**, 289 (2012).
- ²N. Mardirossian and M. Head-Gordon, *Mol. Phys.* **115**, 2315 (2017).
- ³L. Schimka, J. Harl, A. Stroppa, A. Grüneis, M. Marsman, F. Mittendorfer, and G. Kresse, *Nat. Mater.* **9**, 741 (2010).
- ⁴R. B. Araujo, G. L. S. Rodrigues, E. C. dos Santos, and L. G. M. Pettersson, *Nat. Chem.* **13**, 6853 (2022).
- ⁵F. Libisch, C. Huang, and E. A. Carter, *Acc. Chem. Res.* **47**, 2768 (2014).
- ⁶C. A. Gaggioli, S. J. Stoneburner, C. J. Cramer, and L. Gagliardi, *ACS Catal.* **9**, 8481 (2019).
- ⁷T. Schäfer, N. Daelman, and N. López, *J. Phys. Chem. Lett.* **12**, 6277 (2021).
- ⁸A. Tajti, P. G. Szalay, A. G. Császár, M. Kállay, J. Gauss, E. F. Valeev, B. A. Flowers, J. Vázquez, and J. F. Stanton, *J. Chem. Phys.* **121**, 11599 (2004).
- ⁹L. A. Curtiss, P. C. Redfern, and K. Raghavachari, *J. Chem. Phys.* **126**, 084108 (2007).
- ¹⁰R. J. Bartlett and M. Musiał, *Rev. Mod. Phys.* **79**, 291 (2007).
- ¹¹H. Stoll, *Phys. Rev. B* **46**, 6700 (1992).
- ¹²B. Paulus, *Phys. Rep.* **428**, 1 (2006).
- ¹³C. Pisani, M. Schütz, S. Casassa, D. Usvyat, L. Maschio, M. Lorenz, and A. Erba, *Phys. Chem. Chem. Phys.* **14**, 7615 (2012).
- ¹⁴G. H. Booth, A. Grüneis, G. Kresse, and A. Alavi, *Nature* **493**, 365 (2013).
- ¹⁵J. Yang, W. Hu, D. Usvyat, D. Matthews, M. Schütz, and G. K.-L. Chan, *Science* **345**, 640 (2014).
- ¹⁶I. Y. Zhang and A. Grüneis, *Front. Mater.* **6** (2019), 10.3389/fmats.2019.00123.
- ¹⁷B. T. Lau, G. Knizia, and T. C. Berkelbach, *J. Phys. Chem. Lett.* **12**, 1104 (2021).
- ¹⁸A. Kubas, D. Berger, H. Oberhofer, D. Maganas, K. Reuter, and F. Neese, *J. Phys. Chem. Lett.* **7**, 4207 (2016).
- ¹⁹J. Sauer, *Acc. Chem. Res.* **52**, 3502 (2019).
- ²⁰J. G. Brandenburg, A. Zen, M. Fitzner, B. Ramberger, G. Kresse, T. Tzatsoulis, A. Grüneis, A. Michaelides, and D. Alfè, *J. Phys. Chem. Lett.* **10**, 358 (2019).
- ²¹M. Alessio, D. Usvyat, and J. Sauer, *J. Chem. Theory Comput.* **15**, 1329 (2019).
- ²²T. Schäfer, A. Gallo, A. Irmmler, F. Hummel, and A. Grüneis, *J. Chem. Phys.* **155**, 244103 (2021).
- ²³T. Mullan, L. Maschio, P. Saalfrank, and D. Usvyat, *J. Chem. Phys.* **156**, 074109 (2022).
- ²⁴B. X. Shi, A. Zen, V. Kapil, P. R. Nagy, A. Grüneis, and A. Michaelides, *J. Am. Chem. Soc.* **145**, 25372 (2023).
- ²⁵H.-Z. Ye and T. C. Berkelbach, *J. Chem. Phys.* **154**, 131104 (2021).
- ²⁶H.-Z. Ye and T. C. Berkelbach, *J. Chem. Phys.* **155**, 124106 (2021).
- ²⁷S. J. Bintrim, T. C. Berkelbach, and H.-Z. Ye, *J. Chem. Theory Comput.* **18**, 5374 (2022).
- ²⁸H.-Z. Ye and T. C. Berkelbach, *J. Chem. Theory Comput.* **18**, 1595 (2022).
- ²⁹Z. Rolik and M. Kállay, *J. Chem. Phys.* **135**, 104111 (2011).
- ³⁰P. R. Nagy and M. Kállay, *J. Chem. Phys.* **146**, 214106 (2017).
- ³¹O. Björnholm, M. H. Hansen, A. Hodgson, L.-M. Liu, D. T. Limmer, A. Michaelides, P. Pedevilla, J. Rossmeisl, H. Shen, G. Tocci, E. Tyrode, M.-M. Walz, J. Werner, and H. Bluhm, *Chem. Rev.* **116**, 7698 (2016).
- ³²R. Mu, Z.-J. Zhao, Z. Dohnálek, and J. Gong, *Chem. Soc. Rev.* **46**, 1785 (2017).
- ³³E. Barry, R. Burns, W. Chen, G. X. De Hoe, J. M. M. De Oca, J. J. de Pablo, J. Dombrowski, J. W. Elam, A. M. Felts, G. Galli, J. Hack, Q. He, X. He, E. Hoenig, A. Iscen, B. Kash, H. H. Kung, N. H. C. Lewis, C. Liu, X. Ma, A. Mane, A. B. F. Martinson, K. L. Mulfort, J. Murphy, K. Møllhave, P. Nealey, Y. Qiao, V. Rozyyev, G. C. Schatz, S. J. Sibener, D. Talapin, D. M. Tiede, M. V. Tirrell, A. Tokmakoff, G. A. Voth, Z. Wang, Z. Ye, M. Yesibolati, N. J. Zaluzec, and S. B. Darling, *Chem. Rev.* **121**, 9450 (2021).
- ³⁴J. Schneider, M. Matsuoka, M. Takeuchi, J. Zhang, Y. Horiuchi, M. Anpo, and D. W. Bahnemann, *Chem. Rev.* **114**, 9919 (2014).
- ³⁵R. Rousseau, V.-A. Glezakou, and A. Selloni, *Nat. Rev. Mater.* **5**, 460 (2020).
- ³⁶K. C. Hass, W. F. Schneider, A. Curioni, and W. Andreoni, *Science* **282**, 265 (1998).
- ³⁷H. Kirsch, J. Wirth, Y. Tong, M. Wolf, P. Saalfrank, and R. K. Campen, *J. Phys. Chem. C* **118**, 13623 (2014).
- ³⁸U. Diebold, *J. Chem. Phys.* **147**, 040901 (2017).
- ³⁹M. A. Henderson, *Surf. Sci.* **355**, 151 (1996).
- ⁴⁰N. G. Petrik, P. L. Huestis, J. A. LaVerne, A. B. Aleksandrov, T. M. Orlando, and G. A. Kimmel, *J. Phys. Chem. C* **122**, 9540 (2018).
- ⁴¹Y. Tong, J. Wirth, H. Kirsch, M. Wolf, P. Saalfrank, and R. K. Campen, *J. Chem. Phys.* **142**, 054704 (2015).
- ⁴²I. M. Brookes, C. A. Muryn, and G. Thornton, *Phys. Rev. Lett.* **87**, 266103 (2001).
- ⁴³Z.-T. Wang, Y.-G. Wang, R. Mu, Y. Yoon, A. Dahal, G. K. Schenter, V.-A. Glezakou, R. Rousseau, I. Lyubintsev, and Z. Dohnálek, *Proc. Natl. Acad. Sci.* **114**, 1801 (2017).
- ⁴⁴V. A. Ranea, I. Carmichael, and W. F. Schneider, *J. Phys. Chem. C* **113**, 2149 (2009).
- ⁴⁵B. Wang, H. Hou, Y. Luo, Y. Li, Y. Zhao, and X. Li, *J. Phys. Chem. C* **115**, 13399 (2011).
- ⁴⁶J. Wirth and P. Saalfrank, *J. Phys. Chem. C* **116**, 26829 (2012).
- ⁴⁷J. P. Perdew, K. Burke, and M. Ernzerhof, *Phys. Rev. Lett.* **77**, 3865 (1996).
- ⁴⁸S. Grimme, J. Antony, S. Ehrlich, and H. Krieg, *J. Chem. Phys.* **132**, 154104 (2010).
- ⁴⁹J. Sun, A. Ruzsinszky, and J. P. Perdew, *Phys. Rev. Lett.* **115**, 036402 (2015).
- ⁵⁰C. Adamo and V. Barone, *J. Chem. Phys.* **110**, 6158 (1999).
- ⁵¹B. Peters, *Reaction rate theory and rare events* (Elsevier, 2017).
- ⁵²M. E. Arroyo-de Dompablo, A. Morales-García, and M. Taravillo, *J. Chem. Phys.* **135**, 054503 (2011).
- ⁵³D. C. Cronemeyer, *Phys. Rev.* **87**, 876 (1952).
- ⁵⁴M. B. Huggenschmidt, L. Gamble, and C. T. Campbell, *Surf. Sci.* **302**, 329 (1994).
- ⁵⁵R. Schaub, P. Thostrup, N. Lopez, E. Lægsgaard, I. Stensgaard, J. K. Nørskov, and F. Besenbacher, *Phys. Rev. Lett.* **87**, 266104 (2001).
- ⁵⁶D. A. Duncan, F. Allegretti, and D. P. Woodruff, *Phys. Rev. B* **86**, 045411 (2012).
- ⁵⁷L. A. Harris and A. A. Quong, *Phys. Rev. Lett.* **93**, 086105 (2004).
- ⁵⁸P. J. D. Lindan and C. Zhang, *Phys. Rev. B* **72**, 075439 (2005).
- ⁵⁹P. J. D. Lindan and C. Zhang, *Phys. Rev. Lett.* **95**, 029601 (2005).
- ⁶⁰L. A. Harris and A. A. Quong, *Phys. Rev. Lett.* **95**, 029602 (2005).
- ⁶¹N. Kumar, P. R. C. Kent, D. J. Wesolowski, and J. D. Kubicki, *J. Phys. Chem. C* **117**, 23638 (2013).
- ⁶²B. Wen, M. F. C. Andrade, L.-M. Liu, and A. Selloni, *Proc. Natl. Acad. Sci.* **120**, e2212250120 (2023).
- ⁶³Z. Zeng, F. Wodaczek, K. Liu, F. Stein, J. Hutter, J. Chen, and B. Cheng, *Nat. Commun.* **14**, 6131 (2023).
- ⁶⁴C. T. Campbell and J. R. V. Sellers, *Chem. Rev.* **113**, 4106 (2013).
- ⁶⁵T. Schäfer, F. Libisch, G. Kresse, and A. Grüneis, *J. Chem. Phys.* **154**, 011101 (2021).
- ⁶⁶S. L. Dudarev, G. A. Botton, S. Y. Savrasov, C. J. Humphreys, and A. P. Sutton, *Phys. Rev. B* **57**, 1505 (1998).
- ⁶⁷F. Noé, A. Tkatchenko, K.-R. Müller, and C. Clementi, *Ann. Rev. Phys. Chem.* **71**, 361 (2020).
- ⁶⁸M. S. Chen, J. Lee, H.-Z. Ye, T. C. Berkelbach, D. R. Reichman, and T. E. Markland, *J. Chem. Theory Comput.*, Article ASAP (2023).
- ⁶⁹Q. Yu, C. Qu, P. L. Houston, A. Nandi, P. Pandey, R. Conte, and J. M. Bowman, *J. Phys. Chem. Lett.* **14**, 8077 (2023).
- ⁷⁰K. Momma and F. Izumi, *J. Appl. Cryst.* **44**, 1272 (2011).

Supplementary Material: *Ab Initio* Surface Chemistry with Chemical Accuracy: Application to Water on Metal Oxides

Hong-Zhou Ye^{*,†} and Timothy C. Berkelbach^{*,†,‡}

[†]*Department of Chemistry, Columbia University, New York, New York 10027, USA*

[‡]*Initiative for Computational Catalysis, Flatiron Institute, New York, NY 10010, USA*

E-mail: hzyechem@gmail.com; t.berkelbach@columbia.edu

Note: figures and equations appearing in the main text will be referred to as “Fig. Mxxx” and “Eq. Mxxx” in this Supplementary Material document.

Contents

S1 Overall computational details	4
S1.1 Geometries	4
S1.2 SCAN+D3, PBE+ <i>U</i> +D3, PBE0+D3, HF, and MP2	5
S1.3 LNO-CCSD(T)	6
S1.4 Adsorption energy calculation	11
S1.5 Vibrational corrections	12
S2 Water on the α-Al₂O₃(0001) surface	13
S2.1 Atomic structure	13
S2.2 Converged energetics	13
S2.3 Slab size, surface size, basis size, and Brillouin zone sampling	14
S2.4 Infinite vacuum correction	18
S2.5 Vibrational corrections	19
S3 Water on the rutile TiO₂(110) surface	21
S3.1 Atomic structure	21
S3.2 Converged energetics	21
S3.3 Slab size, surface size, basis size, and Brillouin zone sampling	22
S3.4 Infinite vacuum correction	26
S3.5 Vibrational corrections	28
S4 Optimized geometries	29
S4.1 Bulk lattice constants	29
S4.2 Optimized geometries	29
S4.3 Energy uncertainty from the geometry	29
S5 Timing	30

S1 Overall computational details

S1.1 Geometries

All geometries are optimized at the PBE(+D3) level of theory using the Quantum Espresso (QE) v6.4 code^{1,2} with an energy convergence threshold of 0.2 meV/cell and a force convergence threshold of 0.05 eV/Å. The projector augmented wave pseudopotentials for PBE as obtained from the QE official site are used for all elements (Table S1). For both surface systems (Al₂O₃ and TiO₂), bulk geometries are first optimized, from which clean surfaces are constructed and optimized. The molecularly and dissociatively adsorbed water-surface geometries are then constructed and optimized, followed by climbing image nudged elastic band (CI-NEB) calculations to find the transition-state (TS) geometries. The D3 dispersion correction by Grimme and co-workers³ is used for the PBE geometry optimization of both clean surfaces and surfaces with adsorbates but not for bulk, where we found the effect of the dispersion correction to be small (see Section S4.1). Other parameters affecting the geometry relaxation, including the plane-wave kinetic energy cut-off, the *k*-point mesh for Brillouin zone sampling, and the size of the slab model are detailed in Section S2 for the Al₂O₃ surface and Section S3 for the TiO₂ surface, respectively. The final optimized geometries are provided in Section S4.2. We also estimate the effect of the employed PBE+D3 geometries on the calculated adsorption and reaction energetics in Section S4.3.

Table S1: The pseudopotential file (as obtained from the Quantum Espresso official site) and valence electrons for each element used by the plane-wave DFT calculations in this work.

Element	PP file	Valence electrons
Al	Al.pbe-n-kjpaw_psl.1.0.0.UPF	$3s^23p^1$
Ti	Ti.pbe-spn-kjpaw_psl.1.0.0.UPF	$3s^23p^63d^2$
O	O.pbe-n-kjpaw_psl.1.0.0.UPF	$2s^22p^4$
H	H.pbe-kjpaw_psl.1.0.0.UPF	$1s^1$

S1.2 SCAN+D3, PBE+U+D3, PBE0+D3, HF, and MP2

Single-point calculations are performed at the PBE+D3-optimized geometries from above using different levels of theory to obtain the adsorption energy, reaction energies, and barrier heights reported in the main text. These single-point calculations were performed using a combination of QE and the PySCF package.⁴⁻⁶ All numbers are carefully converged to within 1 kcal/mol with respect to the basis set size, the surface size, the slab size, and Brillouin zone sampling, as detailed in Sections S2 and S3 for the two surface systems, respectively. The D3 dispersion correction is included in all reported DFT energies (PBE, SCAN, PBE0, and PBE+U). For PBE and PBE+U, we use the D3 energy for PBE calculated from QE. For SCAN (whose D3 parameters are not available in QE) and PBE0 (for which we performed calculations with PySCF), we calculate the respective D3 energies using the `simple-dftd3` code (<https://github.com/dftd3/simple-dftd3>), and we verified that this code gives the same D3 energy for PBE compared to QE.

The PBE+U calculations are performed using QE with the simplified version of Cococcioni and de Gironcoli⁷ (`lda_plus_u_kind = 0`) and the atomic projector (`U_projection_type = 'atomic'`). The SCAN calculations are performed using QE with the norm-conserving Hartwigsen-Goedecker-Hutter (HG) pseudopotentials^{8,9} optimized for PBE. All other calculations, including the wavefunction calculations and the hybrid DFT calculations with the PBE0 functional, are performed using the PySCF code⁴⁻⁶ with translational symmetry-adapted Gaussian basis functions. The Goedecker-Teter-Hutter (GTH) pseudopotentials optimized for HF¹⁰ or PBE^{8,9} (for PBE0 only) are employed, with the same number of valence electrons as listed in Table S1. The correlation-consistent Gaussian basis set series optimized for the GTH pseudopotentials from Ref. 11, GTH-cc-pVXZ with $X = D, T, Q$ (henceforth denoted by XZ), are used for all elements except for Ti, for which we performed similar basis optimization as in Ref. 11 to generate the corresponding GTH-cc-pVXZ series. We verified at PBE level that the reaction energetics calculated from PySCF agree within 1 kcal/mol with those from QE when using a TZ basis set. The four-center electron-repulsion integrals are handled using the fast periodic density fitting algorithm from Ref. 12–14. The fitting basis sets are optimized for the GTH-cc-pVXZ series of these elements by

minimizing the error of HF and MP2 energies of molecular monohydrides. We verified that the error in the calculated reaction energetics (from both mean-field and correlated calculations) introduced by these optimized fitting basis sets are less than 0.1 kcal/mol by comparing to a large even-tempered fitting basis set generated by PySCF. All basis set data can be found in https://github.com/hongzhouye/supporting_data/tree/main/2023/arXiv%3A2309.14640.

For HF and PBE0 calculations, the finite-size error of the exact, nonlocal exchange energy arising from the integrable divergence at $\mathbf{G} = \mathbf{0}$ is treated using a Madelung constant correction 15–17. This yields an energy with an asymptotic $1/N_k$ convergence to the thermodynamic limit (TDL), with N_k the number of k -points used to sample the Brillouin zone. These “finite-size error-corrected” orbital energies are used to obtain both the MP2 correlation energy and the (T) part of the CCSD(T) correlation energy. In contrast, CCSD calculations are independent of the use of Madelung constant corrections, as long as they are consistently applied.

S1.3 LNO-CCSD(T)

LNO-CCSD(T) calculations are performed using an in-house implementation in a developer version of PySCF based on the molecular LNO-CCSD(T) theory by Kállay and co-workers.^{18–20} In PySCF, most methods implemented for molecular calculations are automatically applicable to solids with Γ -point Brillouin zone sampling by replacing the preceding molecular mean-field calculations (HF in our case) with the corresponding periodic version. For the general case where the Brillouin zone is sampled by an evenly spaced, Γ -included k -point mesh, we first transform the k -point HF orbitals in the original simulation cell into the corresponding Γ -point HF orbitals in the BvK supercell and then perform LNO-CCSD(T) calculations therein.

For completeness, we briefly review the LNO-CCSD(T) theory here and guide the reader to the original publications^{18–20} for details. All systems studied in this work are closed-shell and described by a spin-restricted HF reference determinant $|\Phi_0\rangle$, with canonical HF orbitals ψ_p , orbital energies ϵ_p , and total energy E_{HF} . We use i, j, k for N_o occupied orbitals, a, b, c for N_v virtual orbitals, and p, q, r, s for N unspecified molecular orbitals. In this basis, the electronic Hamiltonian

is

$$H = \sum_{pq,\sigma}^N h_{pq} a_{p\sigma}^\dagger a_{q\sigma} + \frac{1}{2} \sum_{pqrs,\sigma\sigma'}^N V_{pqrs} a_{p\sigma}^\dagger a_{q\sigma'}^\dagger a_{s\sigma'} a_{r\sigma} \quad (\text{S1})$$

with $V_{pqrs} = (pq|rs)$ in (11|22) notation.

We choose the generalized Pipek-Mezey method²¹ with a minao projector to localize the HF occupied orbitals

$$\phi_I = \sum_i^{N_o} U_{iI} \psi_i \quad (\text{S2})$$

Representative localized occupied orbitals are shown in Fig. M1C for water-Al₂O₃ and M3B for water-TiO₂. For each localized occupied orbital, ϕ_I , one constructs a local active space \mathcal{P}_I by augmenting ϕ_I with selected LNOs from second-order Møller-Plesset perturbation theory²² (MP2). Specifically, one computes the occupied-occupied and the virtual-virtual blocks of the MP2 density matrix

$$D_{ij}^I = \sum_{ab} t_{ialb}^{(1)} [2t_{jalb}^{(1)} - t_{Iajb}^{(1)}] \quad (\text{S3})$$

$$D_{ab}^I = \sum_{jc} t_{Iajc}^{(1)} [2t_{Ibjc}^{(1)} - t_{jbIc}^{(1)}] \quad (\text{S4})$$

where

$$t_{Iajb}^{(1)} = \frac{(Ia|jb)}{\tilde{\epsilon}_I + \epsilon_j - \epsilon_a - \epsilon_b} \quad (\text{S5})$$

is an approximate MP2 amplitude with $\tilde{\epsilon}_I = \langle \phi_I | f | \phi_I \rangle$, and f is the Fock operator. Diagonalizing the virtual-virtual block

$$D_{ab}^I = \sum_c \xi_c^I X_{ac}^I X_{bc}^I, \quad (\text{S6})$$

gives the virtual LNOs associated with ϕ_I , i.e., $\phi_b = \sum_c X_{cb}^I \psi_c$. For the occupied LNOs, we follow Ref. 18 and diagonalize

$$\tilde{D}_{ij}^I = \sum_{kl} Q_{ik}^I D_{kl}^I Q_{lj}^I = \sum_k^{N_o-1} \xi_k^I X_{ik}^I X_{jk}^I \quad (\text{S7})$$

where $Q_{ij}^I = \delta_{ij} - U_{iI} U_{jI}$ projects out ϕ_I from D_{ij}^I to prevent it from mixing with other occupied

orbitals, giving the occupied LNOs $\phi_j = \sum_k X_{kj}^I \psi_k$. The eigenvalues ξ_p^I , which are between 2 and 0, quantify the importance of a given LNO to the electron correlation of localized orbital ϕ_I . In practice, we construct the local active space \mathcal{P}_I by keeping those LNOs satisfying

$$\xi_i \geq \lambda_0, \quad \xi_a \geq \lambda_v, \quad (\text{S8})$$

for some user-selected thresholds λ_0 and λ_v , producing $n = n_0 + n_v$ orbitals. Typically, n is much less than N and, for gapped systems such as the surface systems studied in this work, does not increase with system size for a targeted level of accuracy. In Fig. [M1C](#) and [M3B](#), we also show the density of the virtual LNOs generated for the representative localized occupied orbitals with $\lambda_v = 10^{-5}$, 10^{-6} , and 10^{-7} .

A local Hamiltonian is then constructed by projecting H into \mathcal{P}_I

$$H_I = \sum_{pq \in \mathcal{P}_I, \sigma} f_{pq}^I a_{p\sigma}^\dagger a_{q\sigma} + \frac{1}{2} \sum_{pqrs \in \mathcal{P}_I, \sigma\sigma'} V_{pqrs} a_{p\sigma}^\dagger a_{q\sigma'}^\dagger a_{s\sigma'} a_{r\sigma} \quad (\text{S9})$$

where

$$f_{pq}^I = h_{pq} + \sum_{j \notin \mathcal{P}_I}^{N_0 - n_0} (2V_{pqjj} - V_{pjij}), \quad (\text{S10})$$

which includes a frozen core contribution. Solving the CCSD amplitude equations with H_I gives the local CCSD amplitudes t_{ia} and t_{iajb} in \mathcal{P}_I , from which the local contribution of the CCSD(T) correlation energy $E^{(I)}$ can be evaluated by

$$E_{\text{CCSD(T)}}^{(I)} = \sum_{kl \in \mathcal{P}_I} U_{kl} [G_{kl}^{(I), \text{CCSD}} + G_{kl}^{(I), \text{(T)}}] U_{ll} \quad (\text{S11})$$

where

$$G_{kl}^{(I), \text{CCSD}} = \sum_{iab \in \mathcal{P}_I} (t_{iakb} + t_{ia} t_{kb}) (2V_{ialb} - V_{ibla}) \quad (\text{S12})$$

and

$$\begin{aligned}
G_{kl}^{(I),(T)} = & -\frac{1}{3} \sum_{a \geq b \geq c \in \mathcal{P}_I} f_{abc} \sum_{ij \in \mathcal{P}_I} \left\{ \right. \\
& w_{ijk}^{abc} \left(+8v_{ijl}^{abc} - 5v_{ikj}^{abc} - 2v_{jil}^{abc} + 2v_{jli}^{abc} + 2v_{lij}^{abc} - 5v_{lji}^{abc} \right) + \\
& w_{ikj}^{abc} \left(-5v_{ijl}^{abc} + 8v_{ilj}^{abc} + 2v_{jil}^{abc} - 2v_{jli}^{abc} - 5v_{lij}^{abc} + 2v_{lji}^{abc} \right) + \\
& \left. w_{kij}^{abc} \left(+2v_{ijl}^{abc} - 5v_{ilj}^{abc} - 5v_{jil}^{abc} + 2v_{jli}^{abc} + 8v_{lij}^{abc} - 2v_{lji}^{abc} \right) \right\}
\end{aligned} \tag{S13}$$

with

$$f_{abc} = \begin{cases} \frac{1}{6}, & a = c, \\ \frac{1}{2}, & a = b \text{ or } b = c, \\ 1, & \text{otherwise,} \end{cases} \tag{S14}$$

$$w_{ijk}^{abc} = W_{ijk}^{abc} / \sqrt{-D_{ijk}^{abc}}, \quad v_{ijk}^{abc} = V_{ijk}^{abc} / \sqrt{-D_{ijk}^{abc}} \tag{S15}$$

$$W_{ijk}^{abc} = P_{ijk}^{abc} \left(\sum_d V_{bdai} t_{kj}^{cd} - \sum_l V_{ckjl} t_{il}^{ab} \right) \tag{S16}$$

$$V_{ijk}^{abc} = W_{ijk}^{abc} + \frac{1}{2} P_{ijk}^{abc} (V_{aibj} t_k^c) \tag{S17}$$

$$D_{ijk}^{abc} = \epsilon_{ii} + \epsilon_{jj} + \epsilon_{kk} - \epsilon_{aa} - \epsilon_{bb} - \epsilon_{cc} \tag{S18}$$

where $P_{ijk}^{abc}(\cdot)$ generates 6-fold permutation

$$P_{ijk}^{abc}(X_{ijk}^{abc}) = X_{ijk}^{abc} + X_{ikj}^{abc} + X_{jik}^{abc} + X_{jki}^{abc} + X_{kij}^{abc} + X_{kji}^{abc} \tag{S19}$$

The remaining correlation contribution from orbitals $\notin \mathcal{P}_I$ can be included at $O(N^5)$ cost by invoking a composite correction at MP2 level, leading to the final expression for the LNO-CCSD(T) total correlation energy

$$E_c = \sum_I^{N_o} \left(E_{\text{CCSD(T)}}^{(I)} - E_{\text{MP2}}^{(I)} \right) + E_{\text{MP2,full}} \tag{S20}$$

where $E_{\text{MP2}}^{(I)}$ is the MP2 correlation energy evaluated in \mathcal{P}_I with H_I and $E_{\text{MP2,full}}$ is the MP2 correla-

tion energy for the entire system. The latter can also be decomposed into contributions from each localized orbital

$$E_{\text{MP2,full}} = \sum_I \sum_{jab} \tilde{t}_{Ia,b}^{(1)} (2V_{Ia,b} - V_{Ib,a}) = \sum_I E_{\text{MP2,full}}^{(I)} \quad (\text{S21})$$

Note that the summation over jab in Eq. (S21) is not restricted to \mathcal{P}_I and $\tilde{t}_{Ia,b}$ is the exact MP2 amplitude for the entire system with one occupied index being transformed into ϕ_I , which is not the same as the approximate local MP2 amplitudes defined in Eq. (S5). Combining Eqs. (S20) and (S21), we obtain the final expression of the LNO-CCSD(T) correlation energy

$$E_c = \sum_I E_{\text{CCSD(T)}}^{(I)} - E_{\text{MP2}}^{(I)} + E_{\text{MP2,full}}^{(I)} = \sum_I E^{(I)}. \quad (\text{S22})$$

For the purpose of calculating reaction energetics as in this work, the local nature of a chemical reaction allows us to further reduce the computational cost by invoking a strategy resembling the spirit of many fragment embedding methods. Specifically, we can choose to use CCSD(T) to evaluate $E^{(I)}$ for only a subset of $M_o \leq N_o$ localized occupied orbitals, with the contributions from the remaining $N_o - M_o$ localized occupied orbitals being accounted for by the MP2 composite correction, leading to a modified energy expression from Eq. (S20)

$$E_c = \sum_I^{M_o} (E_{\text{CCSD(T)}}^{(I)} - E_{\text{MP2}}^{(I)}) + E_{\text{MP2,full}}. \quad (\text{S23})$$

The final reaction energetics calculated from Eq. (S23) thus need to be converged with respect to both the LNO truncation parameters defined in Eq. (S8) and the embedded cluster size M_o . We detail the convergence of reaction energetics for the two systems studied in this work in Sections S2.3 and S3.3, respectively.

Summarizing the steps and cost of an LNO calculation, there are three parts.

1. Full-system MP2, which is required by both the LNO construction [Eqs. (S3)–(S7)] and the MP2 composite correction [Eq. (S20)] and scales as $O(N^5)$.
2. N_o independent integral transformations, which are required by the local Hamiltonian con-

struction [Eq. (S9)] and scale as $O(N^4n)$ each, but embarrassingly parallel in N_0 .

3. Independent correlated calculations of all local Hamiltonians, which scale as N_0 times the cost of a calculation at the desired level of theory in the local active space, i.e., n^6 for CCSD and n^7 for CCSD(T).

For the LNO-CCSD(T) calculations generating the final numbers reported in the main text, solving the local Hamiltonians consists of 90% of the CPU time and hence dominates the computational cost. This is due to the relatively large number of LNOs kept in the subspace for fully converging the calculated energetics to an accuracy well within 1 kcal/mol, as discussed in the main text. For calculations of an even larger system or with a looser LNO truncation threshold, the $O(N^5)$ steps may dominate the computational cost. Although not explored in this work, many numerical techniques such as local domain-based approximations¹⁹ and Laplace transform methods²⁰ have been exploited to make these steps linear scaling for molecular LNO-CCSD(T) calculations. Such advances can also be extended to the periodic LNO-CCSD(T) described here.

S1.4 Adsorption energy calculation

The adsorption energies from PBE0+D3, MP2 and LNO-CCSD(T) are calculated as follows in PySCF

$$E_{\text{ads}} = E_{\text{int}} + E_{\text{surf-relax}} + E_{\text{mol-relax}} \quad (\text{S24})$$

where

$$E_{\text{int}} = E(\text{surf} + \text{mol}) - E(\text{surf} + \text{ghost-mol}) - E(\text{ghost-surf} + \text{mol}) \quad (\text{S25})$$

is the adiabatic interaction energy corrected for the basis set superposition error,

$$E_{\text{surf-relax}} = E(\text{surf}) - E[\text{surf}(\text{relaxed})] \quad (\text{S26})$$

is the surface relaxation energy, and

$$E_{\text{mol-relax}} = E(\text{mol}) - E[\text{mol}(\text{relaxed})] \tag{S27}$$

is the molecular relaxation energy. Both E_{int} and $E_{\text{surf-relax}}$ are evaluated with periodic boundary conditions, while $E_{\text{mol-relax}}$ is evaluated using the molecular code with the same GTH pseudopotential used for the periodic calculations.

S1.5 Vibrational corrections

We evaluate the vibrational zero-point energy

$$\text{ZPE} = \sum_{\alpha} \frac{1}{2} \hbar \omega_{\alpha} \tag{S28}$$

and the temperature-dependent vibrational free energy

$$A_{\text{vib}}(T) = -RT \sum_{\alpha} \ln \frac{e^{\beta \hbar \omega_{\alpha} / 2}}{e^{\beta \hbar \omega_{\alpha}} - 1} \tag{S29}$$

using the phonon frequencies $\{\omega_{\alpha}\}$ calculated at the PBE level using the density functional perturbation theory²³ (DFPT) as implemented in QE. The adsorption energies, reaction energies, and barrier heights reported in Fig. M2A, M3D and M3F include the ZPE correction. The (inverse) reaction rates reported in Fig. M2B include the contribution from $A_{\text{vib}}(T)$.

To reduce the high computational cost of the DFPT calculations, we (i) use slab models that are smaller compared to those used in the electronic structure calculations and (ii) freeze a few layers from the bottom, as detailed in Sections S2.5 and S3.5 for the two surface systems. The D3 dispersion correction is not included in the DFPT calculations because QE does not support calculating its Hessian. However, we verified that all active phonon modes for non-transition state structures and all but one phonon modes for the transition state structures have positive frequencies.

S2 Water on the $\alpha\text{-Al}_2\text{O}_3(0001)$ surface

S2.1 Atomic structure

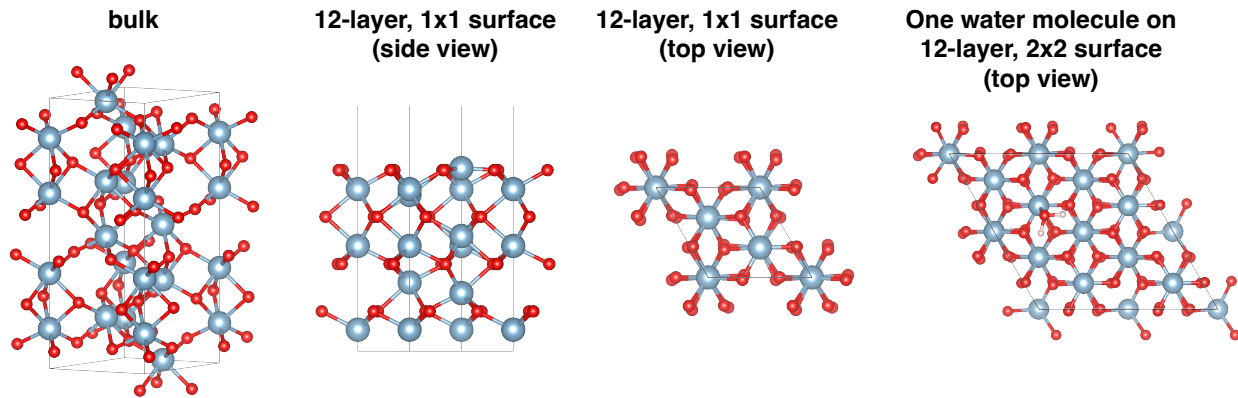


Figure S1: Atomic structure of bulk $\alpha\text{-Al}_2\text{O}_3$, clean $\alpha\text{-Al}_2\text{O}_3(0001)$ surface, and water on 2×2 $\alpha\text{-Al}_2\text{O}_3(0001)$ surface.

The atomic structures of bulk $\alpha\text{-Al}_2\text{O}_3$, clean $\alpha\text{-Al}_2\text{O}_3(0001)$ surface, and water on 2×2 $\alpha\text{-Al}_2\text{O}_3(0001)$ surface are shown in Fig. S1. Following conventions in literature,^{24–27} each atomic layer is counted as a layer in the slab model. This is different from the convention used for the rutile $\text{TiO}_2(110)$ surface (see Section S3.1).

S2.2 Converged energetics

The final numbers for the ZPE-corrected adsorption energy E_{ads} , reaction energy ΔE , and barrier ΔE^\ddagger for the water dissociation on $\alpha\text{-Al}_2\text{O}_3(0001)$ surface reported in Fig. M2A are tabulated in Table S2. These numbers are obtained by combining the energetics from calculations with a finite vacuum size of 23 Å in the direction perpendicular to the slab and a correction to account for an infinite vacuum size (Δ_∞). As detailed in the rest of this section, these numbers have been converged to accuracy within 1 kcal/mol. The convergence with respect to basis size, slab/surface size, and Brillouin zone sampling, which gives rise to the numbers listed in column “23 Å vacuum” in Table S2, is detailed in Section S2.3. The correction to account for an infinite vacuum, which gives rise to the numbers in column “ Δ_∞ ”, is discussed in Section S2.4. The ZPE correction

evaluated in the harmonic approximation using PBE is discussed in Section [S2.5](#).

S2.3 Slab size, surface size, basis size, and Brillouin zone sampling

We follow Ref. [24](#) and other previous DFT studies (e.g., Refs. [25–28](#)) of the same system for the notation of slab size (in terms of the number of atomic layers) and surface size. We will use a notation (n, m) for a slab of n layers, with the top m layers being allowed to relax during geometry optimization. A vacuum of 23 Å perpendicular to the slab plane is used throughout this section. The determination of a correction to account for the infinite vacuum limit is detailed in Section [S2.4](#).

PBE+D3 and SCAN+D3. By first fixing the slab size to be (12, 8), we determined from Table [S3](#) the following converged parameters for the plane wave PBE+D3 calculations:

- a kinetic energy cutoff of 50 Hartree or 1350 eV,
- a surface size of 2×2 ,
- Brillouin zone sampling at the Γ point.

By fixing these parameters and scanning over different slab sizes, we determined from Table [S4](#) a converged slab size of (12, 8). These parameters are also used for the SCAN+D3 calculations, except that we use a higher kinetic energy cutoff of 2000 eV due to the harder pseudopotential.

PBE0+D3 and MP2. By fixing the slab size to be (9, 5), we determined from Table [S5](#) that a TZ Gaussian basis set is sufficient for converged energetics for both mean-field (HF and PBE) and correlated (MP2) calculations. The same table also confirms that the PBE+D3 energetics from PySCF with the TZ Gaussian basis set agrees with the plane wave PBE+D3 numbers from Quantum Espresso (the remaining difference, which is less than 1 kcal/mol, is mostly caused by the use of different pseudopotentials). By fixing the basis set and scanning over different slab sizes, we verified with data in Table [S6](#) that the (12, 8) slab, which converges the PBE+D3 energetics as concluded from Table [S4](#), is also sufficient to converge the MP2 energetics. Finally, we also expect

Table S2: Final numbers (highlighted in grey) for the ZPE-corrected adsorption energy E_{ads} , reaction energy ΔE , and barrier height ΔE^\ddagger for a single water molecule adsorption and dissociation on the $\alpha\text{-Al}_2\text{O}_3(0001)$ surface calculated using different methods as reported in Fig. M2A. Columns labelled by “23 Å” list the regular total electronic energy contributions using a supercell with a vacuum of 23 Å in the z -direction (see Section S2.3). Columns labelled by “ Δ_∞ ” list the estimated infinite vacuum correction (see Section S2.4). Columns labelled by “ZPE” list the zero-point energy correction (see Section S2.5). All numbers are in kcal/mol.

Method	E_{ads}				ΔE				ΔE^\ddagger			
	23 Å	Δ_∞	ZPE	Final	23 Å	Δ_∞	ZPE	Final	23 Å	Δ_∞	ZPE	Final
PBE+D3	-29.21	-0.62	0.42	-29.41	-9.29	1.35	-0.62	-8.56	4.51	0.52	-2.21	2.82
PBE0+D3	-29.87	-0.62	0.42	-30.07	-9.17	1.35	-0.62	-8.44	6.22	0.52	-2.21	4.53
SCAN+D3	-30.40	-0.62	0.42	-30.60	-8.94	1.35	-0.62	-8.21	5.68	0.52	-2.21	3.99
MP2	-26.03	-0.74	0.42	-26.35	-9.07	2.05	-0.62	-7.64	7.03	0.75	-2.21	5.57
CCSD(T)	-26.22	-0.74	0.42	-26.54	-8.93	2.05	-0.62	-7.50	8.07	0.75	-2.21	6.61

Table S3: PBE+D3 dissociation energy ΔE_{diss} and the barrier height ΔE^\ddagger (both in kcal/mol) of a single adsorbed water on the $\alpha\text{-Al}_2\text{O}_3(0001)$ surface evaluated for a (12, 8) slab model with different kinetic energy cutoff (in Hartree), surface size, and Brillouin zone sampling. The parameters that converge both energies within 1 kcal/mol are highlighted in grey.

K.E. cutoff	surface	k -point mesh	ΔE_{diss}	ΔE^\ddagger
50	2×2	$1 \times 1 \times 1$	-9.3	4.6
100	2×2	$1 \times 1 \times 1$	-9.3	4.6
100	2×2	$2 \times 2 \times 1$	-9.3	4.6
50	3×3	$1 \times 1 \times 1$	-9.0	4.6

Table S4: Same reaction energetics as in Table S3 for different choices of slab size. All other parameters are fixed at their optimum values determined in Table S3. The slab size that converge both energies within 1 kcal/mol is highlighted in grey.

Slab size	ΔE_{diss}	ΔE^\ddagger
(12,5)	-9.0	4.4
(12,7)	-9.2	4.6
(12,8)	-9.3	4.6
(15,10)	-9.4	4.6

these parameters (TZ basis set and (12, 8) slab) to be sufficient for PBE0+D3 calculations, as the PBE0 energy is a mixture of the PBE energy and the HF exchange energy.

Table S5: Reaction energetics (in kcal/mol) from HF, MP2, and PBE+D3 calculated using PySCF with the GTH-cc-pVXZ basis sets for a (9, 5)/ 2×2 surface model with Γ -point Brillouin zone sampling. A TZ basis set (highlighted in grey) is sufficient to converge reaction energetics to within 1 kcal/mol for both mean-field (HF, PBE, and hence also PBE0) and correlated (MP2) calculations. The basis-set converged PBE+D3 reaction energetics also agree with those from plane wave/Quantum Espresso very well (the small difference is likely caused by the difference in pseudopotentials).

Basis set	HF		MP2		PBE	
	ΔE_{diss}	ΔE^\ddagger	ΔE_{diss}	ΔE^\ddagger	ΔE_{diss}	ΔE^\ddagger
DZ/PySCF	-13.6	12.6	-8.4	7.2	-7.6	5.0
TZ/PySCF	-13.6	13.5	-8.7	7.2	-8.7	5.3
QZ/PySCF	-13.6	13.5	-8.7	7.2	-8.7	5.3
PW/QE					-9.0	4.7

LNO-CCSD(T). As detailed in Section S1.3, we use Eq. (S23) to evaluate the LNO-CCSD(T)

Table S6: Reaction energetics (in kcal/mol) from MP2 calculated for different slab models using a TZ basis set and for a 2×2 surface model with Γ -point Brillouin zone sampling. As in Table S4, the same (12, 8) slab model is sufficient to converge the MP2 energy.

Slab	ΔE_{diss}	ΔE^{\ddagger}
(12,5)	-9.1	7.1
(12,7)	-9.0	7.2
(12,8)	-9.1	7.0
(15,10)	-9.1	7.4

reaction energetics, which must be converged with respect to both the LNO truncation parameter, λ_o and λ_v , defined in Eq. (S8), and the “embedded” cluster size, M_o , defined in Eq. (S23). For the LNO truncation parameters, we follow Ref. 19 and scan λ_v while keeping $\lambda_o = 10\lambda_v$. For the embedded cluster size M_o , we note that the localized occupied orbitals (LOs) for this system fall into two classes: 4 LOs on the water molecule and 48 LOs for every layer of oxygen atoms (there are no LOs localized on aluminum due to the electron negativity difference between aluminum and oxygen). This results in a natural way of systematically increasing M_o :

1. LOs on the water molecule only, $M_o = 4$,
2. plus LOs on the first oxygen layer, $M_o = 4 + 48 = 52$,
3. plus LOs on the second oxygen layer, $M_o = 4 + 48 + 48 = 100$,
4. plus LOs on the third oxygen layer, $M_o = 4 + 48 + 48 + 48 = 148$,
5. plus LOs on the third oxygen layer, $M_o = 4 + 48 + 48 + 48 + 48 = 196 = N_o$.

The convergence with respect to M_o for different choices of λ_v is shown in Fig. S2 for a (12, 8)/ 2×2 surface model using a TZ basis set. For both the adsorption energy and the barrier height, convergence to an accuracy better than 1 kcal/mol is achieved using even the 4 LOs on the water molecule, while the reaction energy shows a slower convergence and requires further including the first oxygen layer (i.e., $M_o = 52$). Nevertheless, for the numbers reported in Table S2 and in the main text, we use the fully converged results from $M_o = 148$. The M_o -converged

reaction energies and barrier heights from different choices of λ_v (marked as stars in Fig. S2) are then plotted in Fig. M1E to investigate the convergence with respect to the LNO truncation, where we also see a fast convergence to the desired accuracy of 1 kcal/mol, as already discussed in the main text. The convergence with respect to surface size, slab thickness, and basis size is presented in Fig. M1G and M1H, from which we determine that the $(12, 8)/2 \times 2$ model and the TZ basis set are sufficient for converging both the reaction energy and the barrier height to chemical accuracy. These parameters are then used to evaluate the adsorption energy without further modifications.

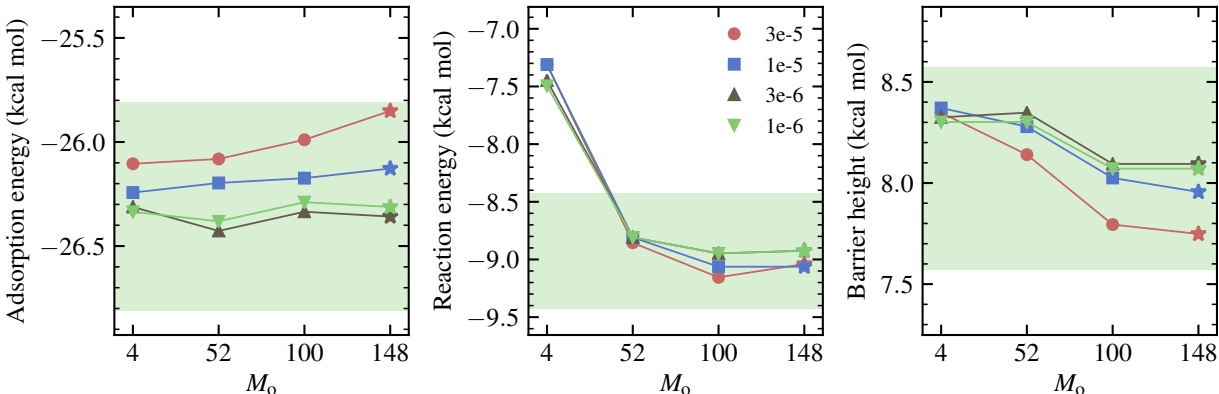


Figure S2: Convergence of the LNO-CCSD(T) adsorption energy (left), reaction energy (middle), and barrier height (right) for water- Al_2O_3 with respect to the embedded cluster size M_0 . A $(12, 8)/2 \times 2$ surface model and a TZ basis set are employed. Data of different color correspond to different virtual LNO truncation parameter λ_v (the occupied truncation parameter is chosen to be $\lambda_o = 10\lambda_v$ in all cases). The range of ± 0.5 kcal/mol from the most converged number (i.e., $\lambda_v = 10^{-6}$ and $M_0 = 148$) is highlighted by the green shaded area.)

S2.4 Infinite vacuum correction

PBE+D3, SCAN+D3, and PBE0+D3. We use the dipole correction at PBE+D3 level as implemented in Quantum Espresso to account for the finite-vacuum effect. For the $(12, 8)$ slab model, we found $\Delta_\infty = -0.62, +1.35,$ and $+0.52$ kcal/mol for the adsorption energy, reaction energy, and barrier height, respectively, as also tabulated in Table S2. These corrections are also applied to obtain the final SCAN+D3 and PBE0+D3 energetics in Table S2.

MP2 and LNO-CCSD(T). For MP2, we manually increase the dimension perpendicular to the

surface (z_{\max}) and repeat the calculations using the (12, 8) model and the TZ basis set. The resulting energies are plotted in Fig. S3, where extrapolation to the infinite vacuum limit using the following function is also shown

$$E(z_{\max}) = \frac{A}{z_{\max} - B} + E(z_{\max} = \infty) \quad (\text{S30})$$

From the plot, we obtain $\Delta_{\infty} = -0.74, 2.05,$ and 0.75 kcal/mol for $E_{\text{ads}}, \Delta E,$ and E^{\ddagger} , respectively, as tabulated in Table S2. In the spirit of the MP2 composite correction, these corrections are also applied to obtain the final LNO-CCSD(T) energetics in Table S2.

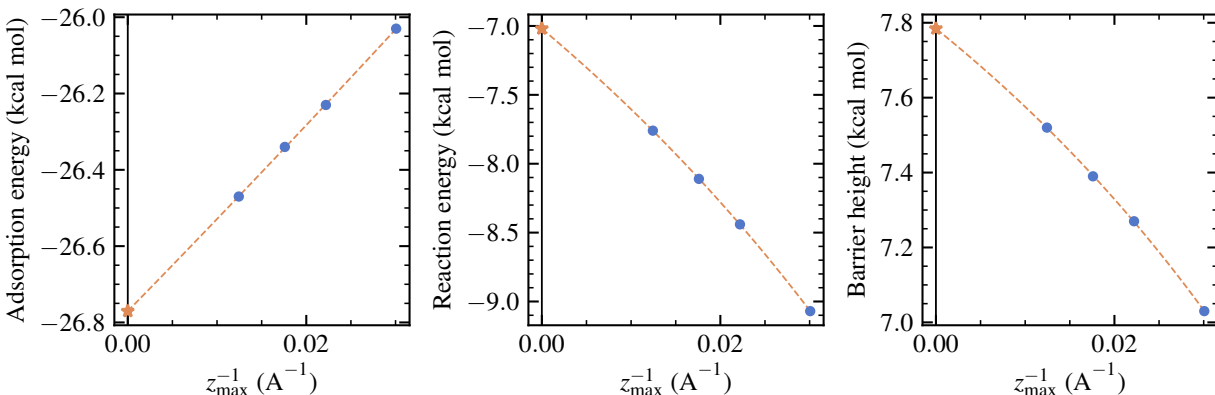


Figure S3: Convergence of the MP2 adsorption energy (left), reaction energy (middle), and barrier height (right) for water- Al_2O_3 as a function of the reciprocal dimension perpendicular to the surface. Extrapolations based on Eq. (S30) are shown in orange.

S2.5 Vibrational corrections

DFPT calculations at PBE level are performed for the clean surface, molecular adsorption, dissociated adsorption, and transition state of a $(9,5)/2 \times 2$ surface model. Atoms in the four layers from the bottom are kept frozen in the DFPT calculations to reduce the computational cost. The reciprocal space is sampled at the Γ -point. The ZPE corrections for the adsorption energy, reaction energy, and barrier height are already listed in Table S2. The temperature-dependent vibrational activation free energy used to evaluate the reaction rates shown in Fig. M2B is plotted in Fig. S4.

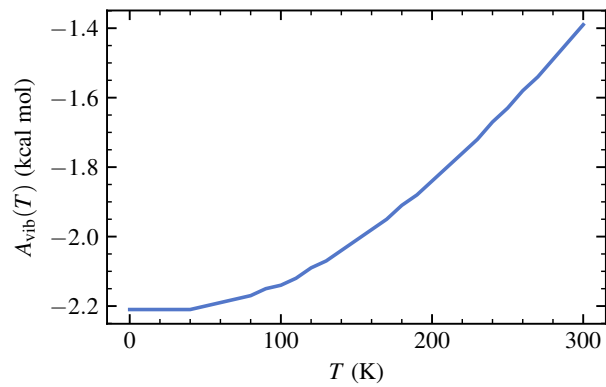


Figure S4: The temperature-dependent vibrational free energy for the barrier height of water dissociation on Al_2O_3 surface calculated according to Eq. (S29).

S3 Water on the rutile $\text{TiO}_2(110)$ surface

S3.1 Atomic structure

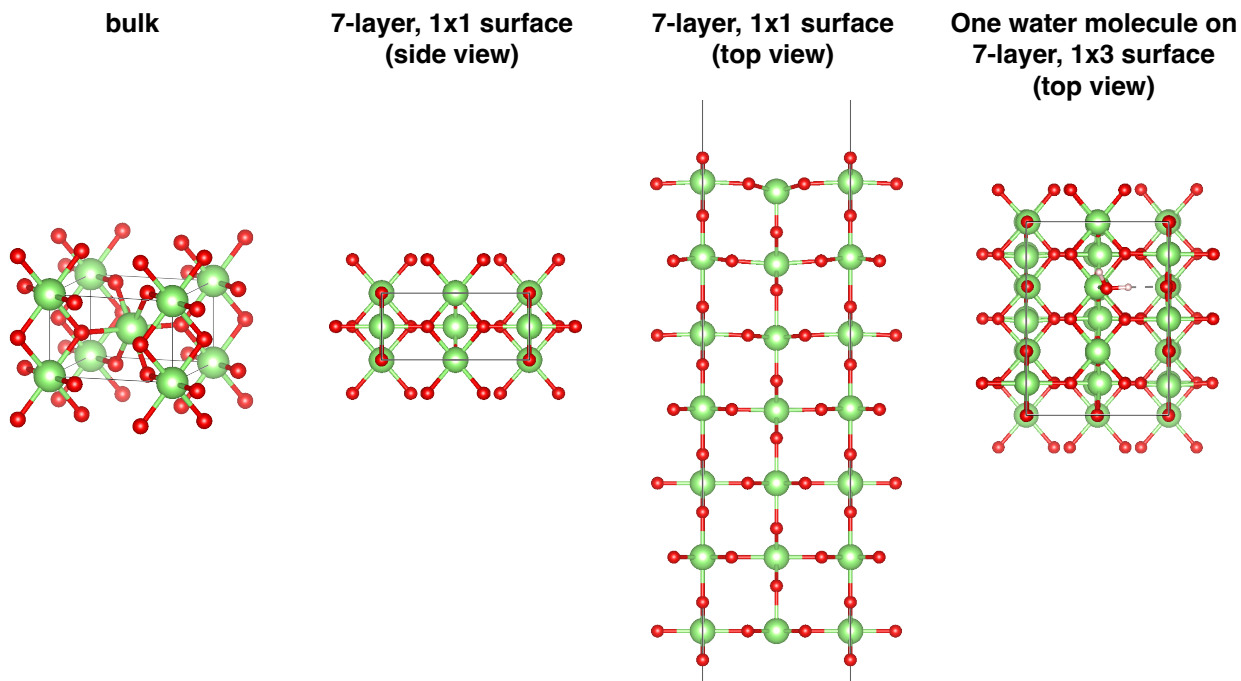


Figure S5: Atomic structure of bulk rutile TiO_2 , clean rutile $\text{TiO}_2(110)$ surface, and water on 1×3 rutile $\text{TiO}_2(110)$ surface.

The atomic structures of bulk rutile TiO_2 , clean rutile $\text{TiO}_2(110)$ surface, and water on 1×3 rutile $\text{TiO}_2(110)$ surface are shown in Fig. S5. The definition of atomic layer follows the literature,^{29–31} where an atomic layer includes a [Ti-O] plane plus the two O planes above and beneath it. Note that this is different from the convention used in Section S2.1 for water on $\alpha\text{-Al}_2\text{O}_3(0001)$ surface.

S3.2 Converged energetics

The final numbers for the ZPE-corrected adsorption energy E_{ads} , reaction energy ΔE , and barrier height ΔE^\ddagger for the water adsorption and dissociation on rutile $\text{TiO}_2(110)$ surface reported in Fig. M3D and M3F are tabulated in Table S7. These numbers are obtained by combining the ener-

getics from calculations with a finite vacuum size of 18 \AA in the direction perpendicular to the slab and a correction to account for an infinite vacuum size (Δ_∞). As detailed in the rest of this section, these numbers have been converged to accuracy within 1 kcal/mol. The convergence with respect to basis size, slab/surface size, and Brillouin zone sampling, which gives rise to the numbers listed in column “ 18 \AA vacuum” in Table S7, is detailed in Section S3.3. The correction to account for an infinite vacuum, which gives rise to the numbers in column “ Δ_∞ ”, is discussed in Section S3.4. The ZPE correction evaluated in the harmonic approximation using PBE is discussed in Section S3.5.

S3.3 Slab size, surface size, basis size, and Brillouin zone sampling

We follow Ref. 30 and other DFT studies on the same system for the notation of slab size and surface size. Like in water- Al_2O_3 , we use a notation (n, m) to denote a slab of n layers, with the top m layers being allowed to relax during geometry optimization

PBE+D3, PBE+ U +D3, and SCAN+D3. Our preliminary tests suggest that a kinetic energy cutoff of 1350 eV and a $2 \times 2 \times 1$ k -point mesh properly converge the basis set size and the Brillouin zone for the PBE+D3 reaction energetics. By fixing these parameters, we determined a converged surface size of 1×3 and a converged slab model of $(7, 4)$ from Fig. S6. The same parameters are used for PBE+ U +D3 and SCAN+D3, except that we use a higher kinetic energy cutoff of 2000 eV for SCAN+D3 due to the harder pseudopotential.

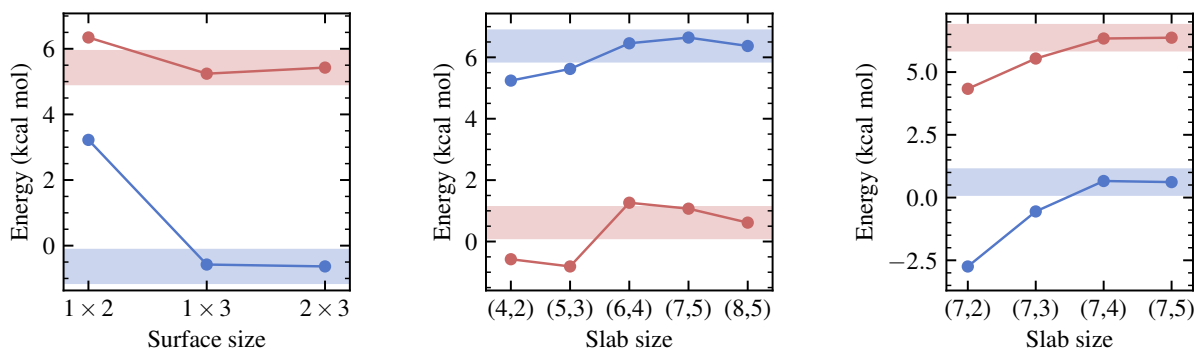


Figure S6: Convergence of the PBE+D3 reaction energy (blue) and barrier height (red) for water dissociation on TiO_2 surface with respect to the surface size (left), the total slab size (middle), and the active slab size (right). A $(4, 2)$ slab model is used for the left panel, while a 1×3 surface model is used for the other two. All calculations were done with the Brillouin zone sampled by a $2 \times 2 \times 1$ mesh.

Table S7: Final numbers (highlighted in grey) for the ZPE-corrected adsorption energy E_{ads} , reaction energy ΔE , and barrier height ΔE^\ddagger for a single water molecule adsorption and dissociation on the rutile $\text{TiO}_2(110)$ surface calculated using different methods as reported in Fig. M3D and M3F. Columns labelled by “18 Å” list the regular total electronic energy contributions using a supercell with a vacuum of 18 Å in the z-direction (see Section S3.3). Columns labelled by “ Δ_∞ ” list the estimated infinite vacuum correction (see Section S3.4). Columns labelled by “ZPE” list the zero-point energy correction (see Section S3.5). All numbers are in kcal/mol.

Method	E_{ads}				ΔE				ΔE^\ddagger			
	18 Å	Δ_∞	ZPE	Final	18 Å	Δ_∞	ZPE	Final	18 Å	Δ_∞	ZPE	Final
PBE+D3	-22.63	0.20	1.40	-21.03	0.65	-0.03	-1.55	-0.93	6.26	-0.09	-2.82	3.35
PBE+U(1)+D3	-21.34	0.20	1.40	-19.74	0.42	-0.03	-1.55	-1.16	5.84	-0.09	-2.82	2.93
PBE+U(3)+D3	-18.60	0.20	1.40	-17.00	-0.16	-0.03	-1.55	-1.74	4.87	-0.09	-2.82	1.96
PBE+U(5)+D3	-15.64	0.20	1.40	-14.04	-0.91	-0.03	-1.55	-2.49	3.69	-0.09	-2.82	0.78
PBE+U(8)+D3	-10.88	0.20	1.40	-9.28	-2.42	-0.03	-1.55	-4.00	1.51	-0.09	-2.82	-1.40
PBE+U(11)+D3	-5.90	0.20	1.40	-4.30	-4.30	-0.03	-1.55	-5.88	-1.06	-0.09	-2.82	-3.97
SCAN+D3	-25.91	0.20	1.40	-24.31	1.31	-0.03	-1.55	-0.27	7.45	-0.09	-2.82	4.54
MP2	-25.65	0.51	1.40	-23.74	0.92	0.07	-1.55	-0.56	9.28	-0.15	-2.82	6.31
CCSD(T)	-22.74	0.51	1.40	-20.83	-0.41	0.07	-1.55	-1.89	7.06	-0.15	-2.82	4.09

MP2. Table S8 suggests that a TZ basis set is sufficient to converge reaction energetics evaluated at both mean-field (HF) and correlated (MP2) level. Table S9 suggests that the HF part of the MP2 energy requires sampling the Brillouin zone with a $2 \times 2 \times 1$ mesh, while the correlation part converges faster and requires only Γ -point Brillouin sampling. Ideally, we thus would like to use the following energy expression for the total MP2 energy

$$E_{\text{MP2}}^{(7,4)}(\text{TZ}/2 \times 2 \times 1) \approx E_{\text{HF}}^{(7,4)}(\text{TZ}/2 \times 2 \times 1) + E_{\text{MP2,c}}^{(7,4)}(\text{TZ}/1 \times 1 \times 1) \quad (\text{S31})$$

However, neither the TZ/2×2×1 HF calculation nor the TZ/1×1×1 MP2 calculation is feasible with the available computational resources. We thus approximate them using the following composite correction

$$\begin{aligned} E_{\text{HF}}^{(7,4)}(\text{TZ}/2 \times 2 \times 1) &\approx E_{\text{HF}}^{(7,4)}(\text{DZ}/1 \times 1 \times 1) \\ &+ \underbrace{E_{\text{HF}}^{(6,4)*}(\text{TZ}/1 \times 1 \times 1) - E_{\text{HF}}^{(6,4)*}(\text{DZ}/1 \times 1 \times 1)}_{\Delta E_{\text{HF}}^{(6,4)*}(\text{TZ}/1 \times 1 \times 1)} \\ &+ \underbrace{E_{\text{HF}}^{(6,4)*}(\text{DZ}/2 \times 2 \times 1) - E_{\text{HF}}^{(6,4)*}(\text{DZ}/1 \times 1 \times 1)}_{\Delta E_{\text{HF}}^{(6,4)*}(\text{DZ}/2 \times 2 \times 1)} \end{aligned} \quad (\text{S32})$$

$$\begin{aligned} E_{\text{MP2,c}}^{(7,4)}(\text{TZ}/1 \times 1 \times 1) &\approx E_{\text{MP2,c}}^{(7,4)}(\text{DZ}/1 \times 1 \times 1) \\ &+ \underbrace{E_{\text{MP2,c}}^{(6,4)*}(\text{TZ}/1 \times 1 \times 1) - E_{\text{MP2,c}}^{(6,4)*}(\text{DZ}/1 \times 1 \times 1)}_{\Delta E_{\text{MP2,c}}^{(6,4)*}(\text{TZ}/1 \times 1 \times 1)} \end{aligned} \quad (\text{S33})$$

where (6, 4)* is derived from the (7,4) slab model by removing one atomic layer from the bottom (this layer was kept frozen during the geometry relaxation). The final MP2 reaction energy and barrier height estimated using Eqs. (S31) to (S33) are shown in Table S10, along with all the energy components.

LNO-CCSD(T). We calculate the LNO-CCSD(T) correlation energy for the (6, 4)* slab model using Eq. (S23) with a MP2 composite correction using the MP2 energy for the (7, 4) slab model calculated by Eq. (S31). The convergence of the LNO-CCSD(T) reaction energetics with respect

Table S8: Reaction energy ΔE and barrier ΔE^\ddagger of water dissociation on TiO_2 for a (4, 2) slab model with 1×2 surface calculated using MP2 with Γ -point Brillouin zone sampling and different Gaussian basis sets. Contributions from the HF and the MP2 correlation energy components to the MP2 energetics are also shown. As highlighted in gray, both the HF energy and the MP2 correlation energy contributions to the reaction energetics converge to accuracy within 1 kcal/mol with a TZ basis set.

Basis set	ΔE			ΔE^\ddagger		
	HF	MP2,c	MP2	HF	MP2,c	MP2
DZ	0.5	6.1	6.6	10.8	0.4	11.2
TZ	-1.1	7.0	5.9	9.9	-0.2	9.7
QZ	-1.4	7.3	5.9	9.7	0.4	10.1

Table S9: Same reaction energetics as in Table S8 but calculated using MP2 with a DZ basis set and different Brillouin zone sampling. Contributions from the HF and the MP2 correlation energy components to the MP2 energetics are also shown. As highlighted in gray, the HF energy converges to accuracy within 1 kcal/mol with $2 \times 2 \times 1$ Brillouin zone sampling, while the MP2 correlation energy converges even faster with Γ -point Brillouin zone sampling.

BZ sampling	ΔE			ΔE^\ddagger		
	HF	MP2,c	MP2	HF	MP2,c	MP2
$1 \times 1 \times 1$	0.5	6.1	6.6	10.8	0.4	11.2
$2 \times 2 \times 1$	-1.5	6.2	4.7	10.7	-0.1	10.6
$3 \times 3 \times 1$	-1.7			10.7		

Table S10: Estimating the MP2 reaction energy and barrier height for the (7,4) slab model using Eqs. (S31) to (S33).

	Slab	Basis set	BZ sampling	E_{ads}	ΔE	ΔE^\ddagger
HF	(7,4)	DZ	$1 \times 1 \times 1$	-15.8	-6.1	9.1
	(6,4)*	DZ	$1 \times 1 \times 1$	-15.6	-5.6	9.2
	(6,4)*	TZ	$1 \times 1 \times 1$	-18.6	-7.1	8.4
	(6,4)*	DZ	$2 \times 2 \times 1$	-7.7	-4.6	9.6
	(6,4)*	Δ TZ	$1 \times 1 \times 1$	1.2	-1.4	-0.8
	(6,4)*	DZ	$\Delta 2 \times 2 \times 1$	6.7	1.0	0.3
	(7,4)	TZ	$\Delta 2 \times 2 \times 1$	-10.9	-6.5	8.6
MP2,c	(7,4)	DZ	$1 \times 1 \times 1$	-17.6	6.0	1.9
	(6,4)*	DZ	$1 \times 1 \times 1$	-17.4	6.2	2.0
	(6,4)*	TZ	$1 \times 1 \times 1$	-17.7	7.7	0.8
	(6,4)*	Δ TZ	$1 \times 1 \times 1$	-0.4	1.4	-1.3
	(7,4)	TZ	$1 \times 1 \times 1$	-17.2	7.4	0.7
MP2	(7,4)	TZ	$2 \times 2 \times 1$	-25.6	0.9	9.3

to the cluster size M_0 is shown in Fig. S7, where the choice of M_0 follows that in water- Al_2O_3 , i.e., the first 4 LOs are localized on water, followed by 72 LOs in each atomic layer. Figure S7 suggests that for all choices of the LNO truncation parameters, $M_0 = 292$, i.e., including LOs in up to the fourth atomic layer is sufficient for a converged results. The converged energetics from using different LNO truncation parameters (marked as stars in Fig. S7) are then plotted in Fig. M3C to investigate the convergence with respect to the LNO truncation, where we also see a fast convergence to the desired accuracy of 1 kcal/mol, as already discussed in the main text.

S3.4 Infinite vacuum correction

PBE+D3, PBE+U+D3, and SCAN+D3. We use the dipole correction at PBE level as implemented in Quantum Espresso to account for the finite-vacuum effect. For the (7,4) slab model, we obtained $\Delta_\infty = 0.20$, -0.03 and -0.09 kcal/mol for the adsorption energy, reaction energy, and barrier height, respectively, as also tabulated in Table S7. These corrections are also applied to obtain the final PBE+U+D3 and SCAN+D3 energetics in Table S7.

MP2 and LNO-CCSD(T). For MP2, we manually increase z_{max} and repeat the calculations using

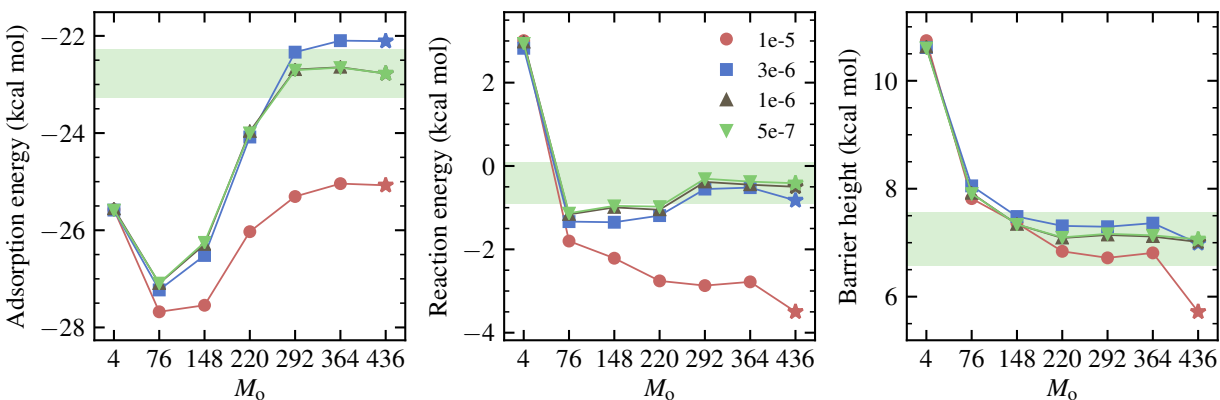


Figure S7: Convergence of the LNO-CCSD(T) adsorption energy (left), reaction energy (middle), and barrier height (right) for water-TiO₂ with respect to the embedded cluster size M_0 . The $(6, 4)^*/1 \times 3$ surface model and the TZ basis set are employed, with a MP2 composite correction evaluated using the $(7, 4)/1 \times 3$ surface model. Data of different color correspond to different virtual LNO truncation parameter λ_v (the occupied truncation parameter is chosen to be $\lambda_o = 10\lambda_v$ in all cases except for $\lambda_v = 5 \times 10^{-7}$, where $\lambda_o = 10^{-5}$). The range of ± 0.5 kcal/mol from the most converged number (i.e., $\lambda_v = 5 \times 10^{-7}$ and $M_0 = 436$) is highlighted by the green shaded area.)

the $(6, 4)^*$ model and the DZ basis set. The resulting energies are plotted in Fig. S8, where extrapolation to the infinite vacuum limit using Eq. (S30) is also shown. From the plot, we obtain $\Delta_\infty = 0.51, 0.07,$ and -0.15 kcal/mol for $E_{\text{ads}}, \Delta E,$ and E^\ddagger , respectively, which are also listed in Table S7. In the spirit of the MP2 composite correction, these corrections are also applied to obtain the final LNO-CCSD(T) energetics in Table S7.

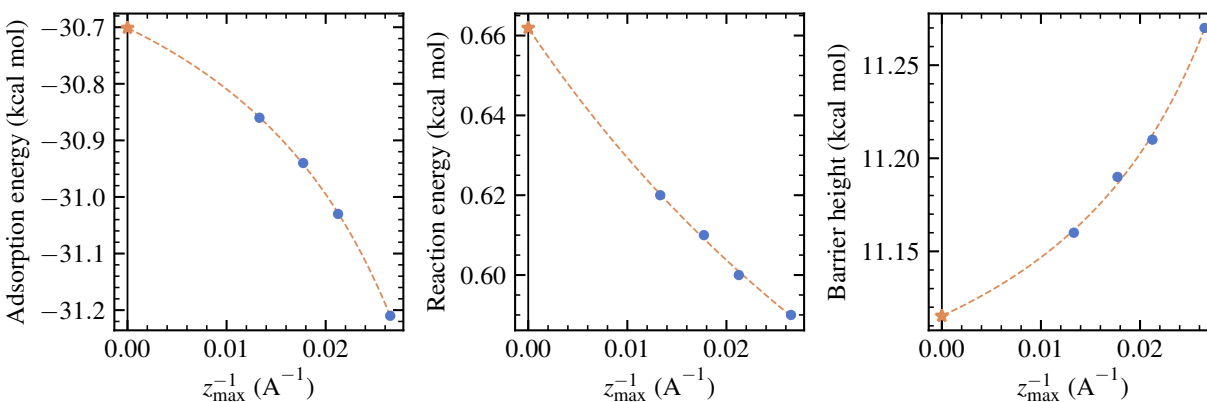


Figure S8: Convergence of the MP2 adsorption energy (left), reaction energy (middle), and barrier height (right) for water-TiO₂ as a function of the reciprocal dimension perpendicular to the surface. Extrapolations based on Eq. (S30) are shown in orange.

S3.5 Vibrational corrections

DFPT calculations at PBE level are performed for the clean surface, molecular adsorption, dissociated adsorption, and transition state of a $(4,2)/1 \times 3$ surface model. Atoms in the three layers from the bottom are kept frozen in the DFPT calculations to reduce the computational cost. The reciprocal space is sampled at the Γ -point in the DFPT calculations. The ZPE corrections for the adsorption energy, reaction energy, and barrier height are already listed in Table [S7](#).

S4 Optimized geometries

S4.1 Bulk lattice constants

Table S11: Optimized lattice constants for bulk α -Al₂O₃ and rutile TiO₂. The PBE geometries are used for the subsequent surface calculations. PBE+D3 geometries are also included for comparison. For both crystals, the difference between PBE and PBE+D3 lattice constants is smaller than 0.4%. $a/b/c$ and $\alpha/\beta/\gamma$ are reported in Å and degree, respectively.

α -Al ₂ O ₃						
	a	b	c	α	β	γ
PBE	4.813	4.813	13.133	90	90	120
PBE+D3	4.796	4.796	13.085	90	90	120
Deviation	0.35%	0.35%	0.37%			
rutile TiO ₂						
	a	b	c	α	β	γ
PBE	4.649	4.649	2.971	90	90	90
PBE+D3	4.636	4.636	2.963	90	90	90
Deviation	0.28%	0.28%	0.27%			

S4.2 Optimized geometries

The PBE+D3 optimized surface geometries can be found in https://github.com/hongzhouye/supporting_data/tree/main/2023/arXiv%3A2309.14640.

S4.3 Energy uncertainty from the geometry

To estimate the uncertainty of the employed PBE+D3 geometry, we repeated the surface geometry relaxation using revPBE³²+D3 and compare the adsorption and reaction energetics evaluated using both the PBE+D3 optimized geometries and the revPBE+D3 optimized geometries. The results are listed in Table S12. We see that in both cases, the difference in the calculated adsorption and reaction energetics due to using the two sets of geometries is well-below chemical accuracy.

Table S12: revPBE+D3 adsorption and reaction energetics evaluated using PBE+D3-optimized geometries and revPBE+D3-optimized geometries. Results from the finite-vacuum geometries are shown without further ZPE or infinite vacuum corrections. All numbers are reported in kcal/mol.

	Geometry	E_{ads}	ΔE	ΔE^\ddagger
$\alpha\text{-Al}_2\text{O}_3(0001)$	PBE+D3	-27.17	-10.23	5.39
	revPBE+D3	-27.22	-10.22	5.43
rutile $\text{TiO}_2(110)$	PBE+D3	-21.63	0.85	7.92
	revPBE+D3	-21.93	1.05	8.10

S5 Timing

The CPU cost for a typical single-point calculation using different methods for water- Al_2O_3 and water- TiO_2 is tabulated in Table S13 and Table S14.

Table S13: CPU cost (unit: hour) for a typical single-point calculation of the water- Al_2O_3 system measured using 16 CPU cores on a single node.

Method	Code	Basis	Slab model	k -point	CPU cost
PBE+D3	QE	100 Ry	(12, 8)/2 × 2	1 × 1 × 1	0.3
SCAN+D3	QE	150 Ry	(12, 8)/2 × 2	1 × 1 × 1	0.5
PBE0+D3	PySCF	TZ	(12, 8)/2 × 2	1 × 1 × 1	42.2
HF	PySCF	TZ	(12, 8)/2 × 2	1 × 1 × 1	30.6
MP2	PySCF	TZ	(12, 8)/2 × 2	1 × 1 × 1	7.4
LNO-CCSD(T)	PySCF	TZ	(12, 8)/2 × 2	1 × 1 × 1	403.4

Table S14: CPU cost (unit: hour) for a typical single-point calculation of the water- TiO_2 system measured using 16 CPU cores on a single node. For HF and MP2, CPU time for the most expensive calculation in the respective protocols is listed.

Method	Code	Basis	Slab model	k -point	CPU cost
PBE+D3	QE	100 Ry	(7, 4)/1 × 3	2 × 2 × 1	4.7
PBE+ U +D3	QE	100 Ry	(7, 4)/1 × 3	2 × 2 × 1	4.3
SCAN+D3	QE	150 Ry	(7, 4)/1 × 3	2 × 2 × 1	49.0
HF	PySCF	DZ	(6, 4)*1 × 3	2 × 2 × 1	1141.9
MP2	PySCF	TZ	(6, 4)*1 × 3	1 × 1 × 1	113.7
LNO-CCSD(T)	PySCF	TZ	(6, 4)*1 × 3	1 × 1 × 1	19099.9

References

- (1) Giannozzi, P.; Baroni, S.; Bonini, N.; Calandra, M.; Car, R.; Cavazzoni, C.; Ceresoli, D.; Chiarotti, G. L.; Cococcioni, M.; Dabo, I.; Corso, A. D.; de Gironcoli, S.; Fabris, S.; Fratesi, G.; Gebauer, R.; Gerstmann, U.; Gougoussis, C.; Kokalj, A.; Lazzeri, M.; Martin-Samos, L.; Marzari, N.; Mauri, F.; Mazzarello, R.; Paolini, S.; Pasquarello, A.; Paulatto, L.; Sbraccia, C.; Scandolo, S.; Sclauzero, G.; Seitsonen, A. P.; Smogunov, A.; Umari, P.; Wentzcovitch, R. M. QUANTUM ESPRESSO: a modular and open-source software project for quantum simulations of materials. *J. Phys. Condens. Matter* **2009**, *21*, 395502.
- (2) Giannozzi, P.; Andreussi, O.; Brumme, T.; Bunau, O.; Nardelli, M. B.; Calandra, M.; Car, R.; Cavazzoni, C.; Ceresoli, D.; Cococcioni, M.; Colonna, N.; Carnimeo, I.; Corso, A. D.; de Gironcoli, S.; Delugas, P.; DiStasio, R. A.; Ferretti, A.; Floris, A.; Fratesi, G.; Fugallo, G.; Gebauer, R.; Gerstmann, U.; Giustino, F.; Gorni, T.; Jia, J.; Kawamura, M.; Ko, H.-Y.; Kokalj, A.; Küçükbenli, E.; Lazzeri, M.; Marsili, M.; Marzari, N.; Mauri, F.; Nguyen, N. L.; Nguyen, H.-V.; de-la Roza, A. O.; Paulatto, L.; Poncé, S.; Rocca, D.; Sabatini, R.; Santra, B.; Schlipf, M.; Seitsonen, A. P.; Smogunov, A.; Timrov, I.; Thonhauser, T.; Umari, P.; Vast, N.; Wu, X.; Baroni, S. Advanced capabilities for materials modelling with Quantum ESPRESSO. *J. Phys. Condens. Matter* **2017**, *29*, 465901.
- (3) Grimme, S.; Antony, J.; Ehrlich, S.; Krieg, H. A consistent and accurate ab initio parametrization of density functional dispersion correction (DFT-D) for the 94 elements H-Pu. *J. Chem. Phys.* **2010**, *132*.
- (4) Sun, Q. Libcint: An efficient general integral library for Gaussian basis functions. *J. Comput. Chem.* **2015**, *36*, 1664–1671.
- (5) Sun, Q.; Berkelbach, T. C.; Blunt, N. S.; Booth, G. H.; Guo, S.; Li, Z.; Liu, J.; McClain, J. D.; Sayfutyarova, E. R.; Sharma, S.; Wouters, S.; Chan, G. K.-L. PySCF: the Python-based simulations of chemistry framework. *Wiley Interdiscip. Rev. Comput. Mol. Sci* **2018**, *8*, e1340.

- (6) Sun, Q.; Zhang, X.; Banerjee, S.; Bao, P.; Barbry, M.; Blunt, N. S.; Bogdanov, N. A.; Booth, G. H.; Chen, J.; Cui, Z.-H.; Eriksen, J. J.; Gao, Y.; Guo, S.; Hermann, J.; Hermes, M. R.; Koh, K.; Koval, P.; Lehtola, S.; Li, Z.; Liu, J.; Mardirossian, N.; McClain, J. D.; Motta, M.; Mussard, B.; Pham, H. Q.; Pulkin, A.; Purwanto, W.; Robinson, P. J.; Ronca, E.; Sayfutyarova, E. R.; Scheurer, M.; Schurkus, H. F.; Smith, J. E. T.; Sun, C.; Sun, S.-N.; Upadhyay, S.; Wagner, L. K.; Wang, X.; White, A.; Whitfield, J. D.; Williamson, M. J.; Wouters, S.; Yang, J.; Yu, J. M.; Zhu, T.; Berkelbach, T. C.; Sharma, S.; Sokolov, A. Y.; Chan, G. K.-L. Recent developments in the PySCF program package. *J. Chem. Phys.* **2020**, *153*, 024109.
- (7) Cococcioni, M.; de Gironcoli, S. Linear response approach to the calculation of the effective interaction parameters in the LDA + U method. *Phys. Rev. B* **2005**, *71*, 035105.
- (8) Goedecker, S.; Teter, M.; Hutter, J. Separable dual-space Gaussian pseudopotentials. *Phys. Rev. B* **1996**, *54*, 1703–1710.
- (9) Hartwigsen, C.; Goedecker, S.; Hutter, J. Relativistic separable dual-space Gaussian pseudopotentials from H to Rn. *Phys. Rev. B* **1998**, *58*, 3641–3662.
- (10) Hutter, J. New Optimization of GTH Pseudopotentials for PBE, SCAN, PBE0 Functionals. GTH Pseudopotentials for Hartree-Fock. NLCC Pseudopotentials for PBE. <https://github.com/juerghutter/GTH>, 2019.
- (11) Ye, H.-Z.; Berkelbach, T. C. Correlation-Consistent Gaussian Basis Sets for Solids Made Simple. *J. Chem. Theory Comput.* **2022**, *18*, 1595–1606.
- (12) Ye, H.-Z.; Berkelbach, T. C. Fast periodic Gaussian density fitting by range separation. *J. Chem. Phys.* **2021**, *154*, 131104.
- (13) Ye, H.-Z.; Berkelbach, T. C. Tight distance-dependent estimators for screening two-center and three-center short-range Coulomb integrals over Gaussian basis functions. *J. Chem. Phys.* **2021**, *155*, 124106.

- (14) Bintrim, S. J.; Berkelbach, T. C.; Ye, H.-Z. Integral-Direct Hartree-Fock and Møller-Plesset Perturbation Theory for Periodic Systems with Density Fitting: Application to the Benzene Crystal. *J. Chem. Theory Comput.* **2022**, *18*, 5374–5381.
- (15) Paier, J.; Marsman, M.; Hummer, K.; Kresse, G.; Gerber, I. C.; Ángyán, J. G. Screened hybrid density functionals applied to solids. *J. Chem. Phys.* **2006**, *124*, 154709.
- (16) Broqvist, P.; Alkauskas, A.; Pasquarello, A. Hybrid-functional calculations with plane-wave basis sets: Effect of singularity correction on total energies, energy eigenvalues, and defect energy levels. *Phys. Rev. B* **2009**, *80*, 085114.
- (17) Sundararaman, R.; Arias, T. A. Regularization of the Coulomb singularity in exact exchange by Wigner-Seitz truncated interactions: Towards chemical accuracy in nontrivial systems. *Phys. Rev. B* **2013**, *87*, 165122.
- (18) Rolik, Z.; Kállay, M. A general-order local coupled-cluster method based on the cluster-in-molecule approach. *J. Chem. Phys.* **2011**, *135*.
- (19) Rolik, Z.; Szegedy, L.; Ladjánszki, I.; Ladóczki, B.; Kállay, M. An efficient linear-scaling CCSD(T) method based on local natural orbitals. *J. Chem. Phys.* **2013**, *139*.
- (20) Nagy, P. R.; Kállay, M. Optimization of the linear-scaling local natural orbital CCSD(T) method: Redundancy-free triples correction using Laplace transform. *J. Chem. Phys.* **2017**, *146*.
- (21) Lehtola, S.; Jónsson, H. Pipek-Mezey Orbital Localization Using Various Partial Charge Estimates. *J. Chem. Theory Comput.* **2014**, *10*, 642–649.
- (22) Møller, C.; Plesset, M. S. Note on an Approximation Treatment for Many-Electron Systems. *Phys. Rev.* **1934**, *46*, 618–622.
- (23) Baroni, S.; de Gironcoli, S.; Dal Corso, A.; Giannozzi, P. Phonons and related crystal properties from density-functional perturbation theory. *Rev. Mod. Phys.* **2001**, *73*, 515–562.

- (24) Hass, K. C.; Schneider, W. F.; Curioni, A.; Andreoni, W. The Chemistry of Water on Alumina Surfaces: Reaction Dynamics from First Principles. *Science* **1998**, *282*, 265–268.
- (25) Hass, K. C.; Schneider, W. F.; Curioni, A.; Andreoni, W. First-Principles Molecular Dynamics Simulations of H₂O on α -Al₂O₃ (0001). *J. Phys. Chem. B* **2000**, *104*, 5527–5540.
- (26) Ranea, V. A.; Carmichael, I.; Schneider, W. F. DFT Investigation of Intermediate Steps in the Hydrolysis of α -Al₂O₃(0001). *J. Phys. Chem. C* **2009**, *113*, 2149–2158.
- (27) Wang, B.; Hou, H.; Luo, Y.; Li, Y.; Zhao, Y.; Li, X. Density Functional/All-Electron Basis Set Slab Model Calculations of the Adsorption/Dissociation Mechanisms of Water on α -Al₂O₃(0001) Surface. *J. Phys. Chem. C* **2011**, *115*, 13399–13411.
- (28) Wirth, J.; Saalfrank, P. The Chemistry of Water on α -Alumina: Kinetics and Nuclear Quantum Effects from First Principles. *J. Phys. Chem. C* **2012**, *116*, 26829–26840.
- (29) Harris, L. A.; Quong, A. A. Molecular Chemisorption as the Theoretically Preferred Pathway for Water Adsorption on Ideal Rutile TiO₂(110). *Phys. Rev. Lett.* **2004**, *93*, 086105.
- (30) Lindan, P. J. D.; Zhang, C. Exothermic water dissociation on the rutile TiO₂(110) surface. *Phys. Rev. B* **2005**, *72*, 075439.
- (31) Wang, Z.-T.; Wang, Y.-G.; Mu, R.; Yoon, Y.; Dahal, A.; Schenter, G. K.; Glezakou, V.-A.; Rousseau, R.; Lyubinetsky, I.; Dohnálek, Z. Probing equilibrium of molecular and deprotonated water on TiO₂(110). *Proc. Natl. Acad. Sci.* **2017**, *114*, 1801–1805.
- (32) Zhang, Y.; Yang, W. Comment on “Generalized Gradient Approximation Made Simple”. *Phys. Rev. Lett.* **1998**, *80*, 890–890.